https://doi.org/10.5194/egusphere-2026-1652
Preprint. Discussion started: 13 May 2026

Assessment of the impact of tropical anthropogenic and biomass-burning emissions on tropospheric ozone (2007–2021) using the GEOS-Chem model constrained by satellite observations

Herizo Narivelo[1], Bastien Sauvage[1], Klaas Folkert Boersma[2,3], Isabelle De Smedt[4], Isidora Anglou[2,3], Michel Van Roozendael[4], Eric Le Flochmoën[1], and Brice Barret[1]

[1]Laboratoire d'Aérologie (LAERO), Université de Toulouse, CNRS, IRD, Toulouse, France
[2]Royal Netherlands Meteorological Institute (KNMI), Satellite Observations department, De Bilt, the Netherlands
[3]Wageningen University, Meteorology and Air Quality group, Wageningen, The Netherlands
[4]Royal Belgian Institute for Space Aeronomy (BIRA-IASB), Brussels, Belgium

Correspondence: Bastien Sauvage (bastien.sauvage@utoulouse.fr)

Abstract. Ozone (O_3) is a secondary species formed and is considered a hazardous pollutant in the troposphere. Over the recent decades, tropospheric O_3 has undergone significant regional variations. This paper focuses on the impact of the evolution of anthropogenic (ANT) and biomass-burning (BB) emissions in the tropics upon tropospheric and the chemical regimes of O_3 using numerical simulations performed of the last 15-years with the GEOS-Chem model. Satellite datasets derived from OMI (HCHO and NO_2) and IASI-SOFRID (CO and O_3) are used as observational constraints to ensure the most reliable representation of BB and ANT emissions. The results show that the simulation (REF) combining GFAS for BB and CAMS for ANT emission provides the best match with the selected satellite observations.

The analysis of REF-simulation shows that positive trends in tropospheric ozone column (TOC) are observed mainly in the Northern Hemisphere (NH), in Asia regions, Temperate North America, Europe, and some tropical regions (Equatorial Asia and Southern Hemisphere (SH) South America), driven by increased of ANT and BB emissions and favourable photochemical conditions.

Sensitivity tests with fixing emissions in the tropical band, reveal that the increase in tropical TOC is mainly due to tropical ANT emissions, which occur in chemical regimes governed by VOC-limited. Further results highlight that effective mitigation of future increases in TOC will depend mostly on control of ANT NOx emissions in tropical regions, where chemical conditions favour high O_3 production, while underlying the marginal role of BB in moderating regional O_3 levels.

1 Introduction

Tropospheric ozone (O_3) is a harmful pollutant to human health (e.g., Brunekreef and Holgate, 2002; WHO, 2003; Bates, 2005) and impacts vegetation growth (Ainsworth et al., 2012; Monks et al., 2015). It is also a potent greenhouse gas particularly important in the upper troposphere (e.g., IPCC, 2007, 2023; Shindell et al., 2006; Stevenson et al., 2013). Tropospheric O_3 is produced by the photochemical oxidation of volatile organic compounds (VOCs) in the presence of nitrogen oxides (NOx).

The temporal variations of tropospheric O_3 over the last few decades is characterised by significant regional variabilities.

https://doi.org/10.5194/egusphere-2026-1652
Preprint. Discussion started: 13 May 2026

Gaudel et al. (2018) highlighted that tropospheric O_3 is the source of important discrepancies between observations and models, particularly in the tropics. Over the last 20-years, O_3 precursor emissions have shifted from the mid-latitudes towards the equator resulting in the increase of the global tropospheric O_3 burden because O_3 photochemistry is favoured in the tropical region (Zhang et al., 2016).

In tropics, strong solar radiation, high temperatures, and abundant biogenic VOC emissions enhance photochemical activity, resulting in O_3 formation features that are different from those observed in mid-latitude regions (Jacob and Winner, 2009). O_3 production in these regions is governed by both VOCs and NOx, as well as their relative abundance. The VOC/NOx ratio is used to characterize the O_3 formation regimes, distinguishing between VOC-limited and NOx-limited conditions (Sillman, 1999). The analysis of this ratio provides key information on the dominant photochemical processes controlling the O_3 formation in tropical regions and enables the implementation of region-specific emission control approaches. In many industrialized NH mid-latitude regions (North America, Europe, China), regulations have led to declining NOx and VOC emissions (e.g., Zheng et al., 2018). Conversely, large increases have been observed in South Asia, Southeast Asia, parts of Africa, and SH South America, due to rapid urbanization, industrialization, and growing energy demand (Granier et al., 2011; Zheng et al., 2018). Biomass-burning (BB) remains a large, variable source of NOx, CO, and VOCs, especially in tropical and subtropical regions, contributing to interannual and seasonal variability (van der Werf et al., 2017; Wang et al., 2025).

Satellite observations and ozonesonde measurements have consistently shown rising trends in tropical tropospheric O_3 over the past two decades. Christiansen et al. (2022) and Froidevaux et al. (2025) report that O_3 increases in the tropical free troposphere, with higher values over regions influenced by BB and ANT activities. Wang et al. (2022) further support these findings by combining IAGOS aircraft data and GEOS-Chem simulations to show significant increases in upper tropospheric O_3, especially between 30°S and 60°N.

Gaudel et al. (2024), show that between 1994 and 2019, tropospheric ozone columns (TOC) increased in the tropics with strongest mid-to-upper tropospheric growth over India, Southeast Asia, and the Malaysia/Indonesia region. Trends in satellite retrieved tropical TOC also exhibit positive increases, especially over Southeast Asia when full sampling is considered. Moreover, studies of regional dynamics (e.g., Stauffer et al., 2024) have suggested that in highly convective tropical regions such as equatorial Southeast Asia, changes in dynamic factors play a role in the observed increase in free tropospheric O_3, occurring alongside growth in local emissions.

The overall increase in O_3 in the troposphere therefore seems mainly coming from the tropics, where NOx emissions are still increasing, although the interactions between emissions, transport and chemistry causing this increase remain poorly understood. As part of the Tropospheric Ozone Assessment Report Phase II (TOAR-II) initiative supported by the International Global Atmospheric Chemistry (IGAC), a working group on O_3 and its precursors in the tropics has been set up to better understand the increase in tropical tropospheric O_3 (https://igacproject.org/opt-focusworking-group). Ozone and some of its precursors have been observed globally by space-based sensors for several decades. In particular, the tropospheric content of nitrogen dioxide (NO_2) and formaldehyde (HCHO) is documented by UV-Visible spectrometers such as GOME-2 (since 2006), OMI (2005-2021), and more recently TROPOMI (2018-now).

Given the difficulty of constructing bottom-up emissions inventories, especially in tropical regions, we use the tropospheric

https://doi.org/10.5194/egusphere-2026-1652
Preprint. Discussion started: 13 May 2026

columns of NO_2 and HCHO products from the European Space Agency Climate Change Initiative (ESA CCI+) consortium to constrain emissions inventories especially in tropical regions, which are more uncertain and less constrained by observations, in order to establish the best possible emissions inventory (anthropogenic (ANT) and biomass-burning (BB)) for the GEOS-Chem global chemistry transport model (CTM). We use NO_2 species because it is a useful proxy for both ANT and BB emissions and directly involved in O_3 production by oxidation of VOCs. Furthermore, in regions affected by pollution, the majority of the NO_2 signal originates from NOx in the boundary layer, produced by combustion processes, and therefore the tropospheric column is a useful indicator of surface emissions (e.g., Martin et al., 2002; Silvern et al., 2019), while HCHO is used as a tracer to further constrain BB emission inventories. The HCHO tropospheric column, as observed from space, is widely used to constrain VOCs emissions from BB, as HCHO is a high-yield tropospheric column to local emissions (e.g., Millet et al., 2006; Gonzi et al., 2011). It also has important biogenic sources (Palmer et al., 2003; Millet et al., 2006). HCHO contributes to the photochemical formation of tropospheric O_3. Although HCHO itself is not a major greenhouse gas, it does contribute indirectly to climate change by reacting in the atmosphere to form compounds that affect the climate.

In addition to NO_2 and HCHO (CCI products), we included CO and O_3 from IASI-SOFRID products in the model-evaluation. CO was taken into account based on its emissions and it has a relatively long atmospheric lifetime of approximately two to three months. This extended lifetime allows CO to be transported over long distances, making it an effective tracer for identifying emission sources at regional to global scales, while O_3 provides insight into the distribution and evolution of global TOC. The main purpose of this study is to assess the impact of the evolution of two surface emissions in the tropics upon tropospheric and chemical regimes of O_3 through numerical simulations of the last 15-years with the GEOS-Chem model using the best emissions inventories for BB and ANT sources.

This paper is structured as follows. Section 2 describes the satellite datasets employed. Section 3 presents the GEOS-Chem configuration, simulation setup and the strategy of the model assessment. Section 4 discusses the main results, including spatial and temporal patterns, as well as comparisons with observations, TOC trends and chemical regime of O_3 production (VOC/NOx ratio) as well as the sensitivity test results, which are based on the best ANT and BB emissions inventories from the model-evaluation. The emissions considered in the sensitivity test on the tropical belt were set at a climate-representative average in order to investigate the impact of tropical emissions on global tropospheric O_3. We focus on the VOC/NOx ratio in order to determine whether the HCHO/NO_2 ratio used in several studies, including O_3 chemical regimes, are the proxy for the VOC/NOx ratio. Furthermore, previous studies have suggested that a change in chemical regimes explains the increase in tropospheric O_3 in mid-latitudes, while its precursors are decreasing. Therefore, we are interested in the VOC/NOx ratio to examine its correlation with TOC trends. Finally, Section 5 summarizes the conclusions.

2 Satellite datasets

2.1 OMI satellite observations

The Ozone Monitoring Instrument (OMI), aboard the NASA's Aura satellite, is a nadir-viewing imaging spectrometer measuring solar backscattered radiation in the UV and VIS spectral ranges (270–500 nm) with a spectral resolution of 0.42–0.63

https://doi.org/10.5194/egusphere-2026-1652
Preprint. Discussion started: 13 May 2026

nm (Levelt et al., 2006, 2018; Kleipool et al., 2022). It provides daily global coverage through a 2600 km swath, with a nominal nadir pixel size of 13 × 24 km^2, increased for affected detector rows following the 2007 row anomaly (Schenkeveld et al., 2017). OMI retrievals of trace gases such as NO_2, O_3, SO_2, and HCHO use the Differential Optical Absorption Spectroscopy (DOAS) technique, with extensive validation against ground-based networks (e.g., Theys et al., 2015; Wang et al., 2017; Ruiz Villena et al., 2020; De Smedt et al., 2021).

In this study, we used the CCI OMI Level 3 (L3) products, which consist of clear-sky sampled monthly mean gridded data (NO_2 and HCHO) at 2°×2.5° of horizontal grids, with improved uncertainty estimates and also monthly mean averaging kernels. For NO_2, we used the OMI version 1 (Anglou et al., 2024), while the HCHO tropospheric columns were obtained from the OMI version 2 (De Smedt et al., 2025).

2.2 IASI-SOFRID data

The Infrared Atmospheric Sounding Interferometer (IASI) are nadir-viewing Fourier transform spectrometers onboard the MetOp-A (2006), MetOp-B (2012) and MetOp-C (2018) satellites (Clerbaux et al., 2009). IASI measures the thermal infrared radiation over the spectral range 645-2760 cm^{-1} with an apodized resolution of 0.5 cm^{-1}, providing twice-daily global coverage with a 2°×2° instantaneous field of view. IASI data are used to provide information about the atmospheric composition, temperature, and humidity. The SOftware for a Fast Retrieval of IASI Data (SOFRID) allows the retrieval of CO and O_3 vertical profiles from IASI radiances. SOFRID-CO has been validated by in situ airborne data from the In-service Aircraft for a Global Observing System (IAGOS) program (De Wachter et al., 2012; Barret et al., 2025), confirming their reliability for global and regional air quality and climate studies. SOFRID-O_3 have also been validated extensively against in-situ data from O_3-sondes from the World Ozone and Ultraviolet Radiation Data Centre (WOUDC) network (Dufour et al., 2012; Barret et al., 2020). Comparisons made with homogenized O_3-sonde data in the latest TOAR assessment report for satellite observations shows that, for TOC, SOFRID-O_3 v3.5 provides the highest correlation coefficients with sonde data in 9 regions out of 14 among 12 global satellite datasets (Hubert et al., in review).

In this paper, we use SOFRID-CO total columns v2.0 (De Wachter et al., 2012) and SOFRID-O_3 tropospheric columns v3.5 (Barret et al., 2020), monthly averaged in 2°×2.5° grids, to complement the model-evaluation.

3 GEOS-Chem model overview, simulation setup, strategy of the model assessment, trend calculation and chemical regime of O_3

3.1 GEOS-Chem model overview

GEOS-Chem (GC) is a global three-dimensional CTM that has been used widely in the atmospheric sciences community for studies of atmospheric composition, air quality, climate–chemistry interactions, long-range transport, and satellite data interpretation (e.g., Bey et al., 2001; Fisher et al., 2011; Whaley et al., 2015; Eastham et al., 2014, 2018; Li et al., 2019; Hammer et al., 2020; Jiang et al., 2022).

https://doi.org/10.5194/egusphere-2026-1652
Preprint. Discussion started: 13 May 2026

GC is an "offline" model, driven by assimilated meteorological fields from NASA's Goddard Earth Observing System (GEOS) (GEOS-FP, MERRA-2), which provide winds, temperature, humidity, and boundary layer parameters at high spatial and temporal resolution (Bey et al., 2001). These datasets ensure that transport processes are consistent with observed atmospheric circulation patterns. GC simulates detailed gas-phase and heterogeneous chemistry, including HOx–NOx–VOC–O_3 interactions, halogen chemistry, and aerosols (Park et al., 2004; Eastham et al., 2014).

GC can be run at different horizontal resolutions from a coarse $4° \times 5°$ global grid to finer $0.5° \times 0.625°$ regional grids and covers both the troposphere and stratosphere. Its 72 vertical levels, with higher resolution near the surface and in the upper troposphere lower stratosphere, capture key processes like boundary-layer mixing, convection, and stratosphere–troposphere exchange (Bey et al., 2001). Photolysis is calculated using the FAST-JX scheme, accounting for clouds, aerosols, and surface reflectivity, which is critical for O_3 and radical formation (Eastham et al., 2014). Chemical transport includes advection, convection, and turbulent mixing to realistically move species from local to global scales (Bey et al., 2001). The GC model includes modules for transport, chemistry, wet and dry deposition, and photolysis (Liu et al., 2001; Wesely, 1989). And finally, the emissions are handled with the HEMCO module (Keller et al., 2014; Lin et al., 2021), incorporating ANT, biogenic, BB, soil, lightning, and volcanic sources with time variations.

3.2 Setup of the reference's simulations

In this paper, we use GEOS-Chem High Performance (GCHP) v14.2.2 (https://geoschem.github.io), the parallelized version of GC for efficient decadal, full-chemistry simulations. All GC simulations are performed from 01 January 2006 to 01 January 2022 on a c48 stretched grid, which corresponds to a nominal global resolution of $2° \times 2.5°$. The "stretched" grid allows finer resolution over regions of interest while maintaining coarser resolution elsewhere. We used 72 vertical levels and meteorological fields from the MERRA-2 reanalysis (Gelaro et al., 2017), providing realistic transport and chemistry throughout the atmosphere.

The biogenic VOC emissions are from MEGAN v2.1 inventory (Guenther et al., 2012) and we use default emissions from other natural sources such as lightning (e.g., Murray et al., 2012; Sauvage et al., 2007), soil NOx (Hudman et al., 2012), volcanoes. Table 1 describes the couple of inventory emissions for the ANT and BB emissions. The first year (2006) of all GC simulation periods is assumed to be a spin-up.

The first simulation named REF1 uses ANT emissions from CEDS v2 (Hoesly et al., 2018) and BB emissions from GFAS (Kaiser et al., 2012). REF2 uses GFAS (BB) and CAMS-ANT v6.2 emissions (Soulie et al., 2024). The REF3 simulation uses FINN v2.5 (Wiedinmyer et al., 2023) as BB emissions and CEDS and the REF4 simulation FINN and CAMS.

The GFAS and FINN are both a global BB emissions inventories, nevertheless, their methods for quantifying these emissions and horizontal resolution are different. The GFAS uses Fire Radiative Power (FRP) from MODIS and scales emissions by fire intensity at $0.5° \times 0.5°$ horizontal resolution (Kaiser et al., 2012) while the FINN emissions inventories uses satellite-detected active fires (MODIS hotspots) and fixed emission factors by vegetation type and fuel load at 1 km of horizontal resolution (Wiedinmyer et al., 2023).

The CEDS emissions was developed for climate and earth system modelling, with a focus on long-term historical consistency

https://doi.org/10.5194/egusphere-2026-1652
Preprint. Discussion started: 13 May 2026

Table 1. Characteristics of the GC simulation. The GFAS and FINN correspond the biomass-burning (BB) emissions, whereas the CEDS and CAMS refer to the anthropogenic (ANT) sources.

Simulations	Couple of emission	Period
REF1	GFAS & CEDS v2	2006 – 2021
REF2	GFAS & CAMS-ANT v6.2	2006 – 2021
REF3	FINN v2.5 & CEDS v2	2006 – 2021
REF4	FINN v2.5 & CAMS-ANT v6.2	2006 – 2021

and the harmonisation of ANT emissions by country, sector and fuel type, for applications ranging from CMIP6 simulations (Hoesly et al., 2018). In contrast, the CAMS has been specifically developed for the operational forecasting of atmospheric composition and air quality reanalyses, by providing emissions with higher resolution (spatial and temporal), suitable for chemical transport models (CTM) and incorporates several datasets, including EDGAR and CEDS, and extends emissions data to recent years using time series and near-real-time updates, which are necessary for forecasting applications (Soulie et al., 2024).

3.3 Strategy of model assessment and choice of the reference simulations

GC simulations are systematically evaluated against the latest satellite observations of tropospheric columns of NO_2 and HCHO retrieved from OMI, and of CO and O_3 retrieved from SOFRID. O_3 is a secondary pollutant which represents one of the main targets of atmospheric chemistry modelling to simulate and forecast regional air quality. O_3 and NO_2 are gathered in the Ox-family as key air quality species because of their oxidation capacity which makes them harmful for human health.

By jointly analysing these species, the evaluation provides a robust constraint on the GC's representation of emissions, chemistry, and transport processes, and helps identify the most consistent emission configuration to better constrain the emissions inventories.

To assess the performance of the GC simulations, we selected several regions across the globe as represented in Fig. 1. Namely, these regions include four oceanic zones, which are used as reference areas with negligible emissions, and a range of continental regions that are representative of either significant ANT NO_2 emissions or major BB emissions.

We also applied the mask defining oceanic and continental regions provided in the satellite products (NO_2 and HCHO) to all regions in the GC simulations for a more accurate comparison between the simulations and observations. The boxes in Fig. 1 delimit the regions to be analysed and evaluated. For example, the SHSAm rectangle covers both oceanic and continental zones, but the mask will only include continental values for SHSAm and other regions with overlapping oceanic and continental zones. The model-evaluation considers only four oceanic regions: SPO, NAO, SAO and IO. The region acronyms are detailed in Fig. 1 caption.

We finally performed statistical analyses of the model versus observations comparisons (Biases and Taylor Diagrams) for the four key species (NO_2, HCHO, O_3 and CO) based on their global and regional (Fig. 1) monthly mean concentrations. We firstly calculate the mean bias error (MBE) which is defined as the difference between the columns of the chemical species (NO_2,

https://doi.org/10.5194/egusphere-2026-1652
Preprint. Discussion started: 13 May 2026

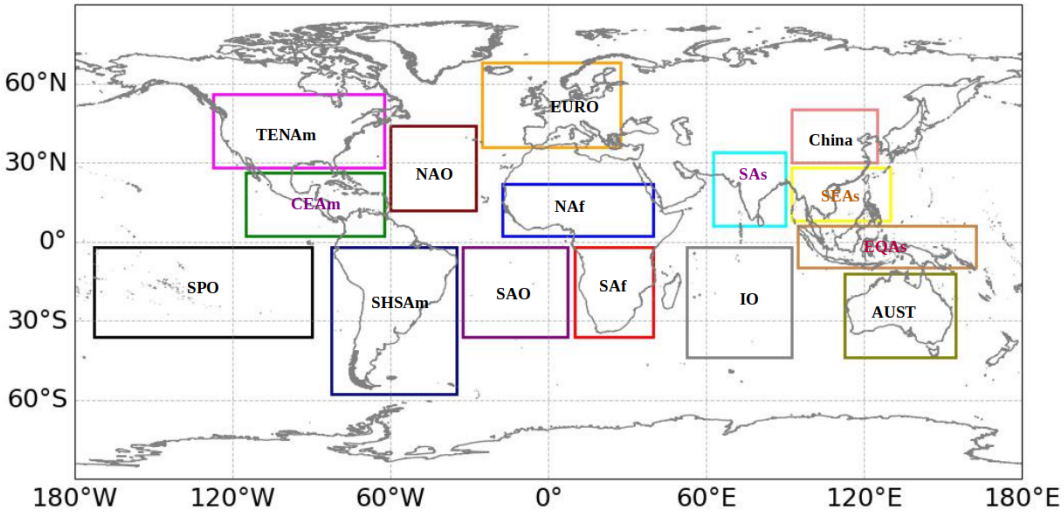

Figure 1. Regional subdomains used for the model output analysis. The defined regions include Southeast Asia (SEAs), South Asia (SAs), Southern Africa (SAf), Northern Africa (NAf), Central America (CEAm), Southern Hemisphere South America (SHSAm), Australia (AUST), China, Equatorial Asia (EQAs), Europe (EURO), Temperate North America (TENAm), and the surrounding oceanic regions: South Pacific Ocean (SPO), South Atlantic Ocean (SAO), and Indian Ocean (IO)

HCHO, CO and O_3) derived from the GC model and those obtained from satellite observations (OMI/IASI). To complement the bias statistical analysis, we use Taylor diagrams in order to evaluate the variabilities of the columns from the different GC simulations relative to the satellite products (OMI/IASI). The Taylor diagram used for climate model validation (Taylor, 2001) takes advantage of the relationship between the Pearson coefficient (R), the Centered Root Mean Square Error (RMSE) and the variabilities (standard deviations) of the two datasets to display these three parameters synthetically.

The RMSE between the GC simulations and OMI (NO_2, HCHO)/SOFRID (CO, O_3) datasets and the standard deviations of the GC simulations results are normalised by the standard deviation of the reference raw OMI/SOFRID data to display the results from multiple regions (Fig. 1) in a single diagram. The reference (here OMI/SOFRID datasets) corresponds to marker 1 on the x-axis (see green star-shaped symbol in Fig. 3). The RMSE is proportional to the distance from this reference point (blue arcs of the circle centered on the reference point). The R between the reference (OMI/SOFRID) and all GC simulation outputs is given by the azimuthal position of the point.

Finally, the radial distance from the origin is proportional to the standard deviation of the GC simulations. Each GC simulation is represented by a different colour, and each region is represented by a marker of a different shape. The better the agreement between GC simulations results and OMI/SOFRID data, the closer the markers will be to the reference point. It helps us to select the couple of emission inventories (ANT and BB inventories emissions) that best matches the observed distributions.

https://doi.org/10.5194/egusphere-2026-1652
Preprint. Discussion started: 13 May 2026

Table 2. Characteristics of the GC sensitivity tests

Simulations	Couple of emission	Period
ANT_Fix	Best ANT emission fixed on tropics (25°N – 25°S) + BB	2006 – 2021
BB_Fix	ANT + best BB emissions fixed on tropics (25°N – 25°S)	2006 – 2021

3.4 Setup of the sensitivity tests

The selection of the most appropriate ANT and BB emission inventories was a crucial step in determining the reference simulation among the four configurations summarized in Table 1. This reference simulation (REF) represents the simulation that best reproduces observed patterns of tropospheric O_3 and its precursors and therefore serves as the foundation for subsequent sensitivity experiments.

To investigate the influence of tropical emissions on global O_3, we defined two sensitivity simulations (Table 2) based on this REF simulation. In these tests, emissions within the tropical band (25°N - 25°S) were fixed to a representative climatological mean, calculated as the average emissions over the first three years of the period (2006–2008) for both BB and ANT emissions inventories. This approach effectively isolates the contribution of interannual changes in tropical emissions. Outside the tropics, emissions were allowed to vary normally according to their year-specific values, thus preserving the temporal evolution of extratropical sources. By contrasting these sensitivity tests with the REF simulation, we can better assess the extent to which emission changes in the tropics have contributed to the observed increase in tropospheric O_3 at both regional and global scales. In addition to the ANT and BB emissions couple summarized in Table 2, all other emissions including natural and other sources were kept consistent with those used in the four GC simulations described in section 3.2.

3.5 Trend calculation and chemical regime of O_3

3.5.1 TOC trend calculation

The TOC temporal variations are different processes at different temporal scales : the annual, biannual and semi-annual cycle, interannual variabilities such as the El Niño-Southern Oscillation (ENSO) and long-term trends. In order to retrieve the long-term trend from our time series we applied the following simplified model (equation 1) (Wespes et al., 2016) to SOFRID and GC TOC monthly time series:

$$TOC(t) = C + A_1.cos(\frac{2\Pi(t-\phi_1)}{12}) + \frac{mt}{12} + A_2.cos(\frac{2\Pi(t-\phi_2)}{24}) + A_3.cos(\frac{2\Pi(t-\phi_3)}{6}) + \alpha.ONI(t) \quad (1)$$

Where:

- t: months
- C: monthly TOC
- $A_1.\cos(\frac{2\Pi(t-\phi_1)}{12})$: annual seasonal cycle (12 months period)

https://doi.org/10.5194/egusphere-2026-1652
Preprint. Discussion started: 13 May 2026

- $A_2.\cos(\frac{2\Pi(t-\phi_2)}{24})$: biannual variability cycle (24 months period)
- $A_3.\cos(\frac{2\Pi(t-\phi_3)}{6})$: semi-annual variation (6-months period)
- $\frac{mt}{12}$: annual linear trend
- ϕ_1, ϕ_2 and ϕ_3 : phase shifts of the respective cosine terms
- α.ONI (t): Oceanic Niño Index (ONI) version 5 (sensitivity to the ENSO events, NOAA Climate Prediction Center website, last access: 24 March 2026).

3.5.2 Diagnostic of chemical regime

The formation of O_3 in the troposphere is a non-linear function of its precursors, mainly nitrogen oxides (NOx = NO + NO_2) and volatile organic compounds (VOCs). It is essential to determine whether O_3 production is limited by NOx or by VOC in order to interpret the factors behind the trends observed in tropical regions. A standard diagnostic approach is to calculate the ratio between the total VOCs and NOx, usually in the following equation (2):

$$chemical\ regime = \frac{\sum VOC}{NOx} \tag{2}$$

Due to the various types of VOCs in the GC model, in the ratio calculation, we only use reactive VOCs such as Isoprene, Toluene, Benzene, Xylene, HCHO, Acetaldehyde and Ethylene. Given to the coarse horizontal resolution ($2° \times 2.5°$) and the diversity of VOC species represented in GC model, we assume that the VOC/NOx > 8 usually indicates a NOx-limited regime while VOC/NOx < 4 corresponds to a VOC-limited regime. VOC/NOx values between these thresholds suggest a transition regime. These thresholds reflect the use of total reactive VOC rather than proxy species and are broadly consistent with observational diagnostics based on the HCHO/NO_2 ratio, which typically place the transition between VOC- and NOx-limited O_3 production in the range of ~2–4 (e.g., Martin et al., 2004; Duncan et al., 2010; Elshorbany et al., 2024). This approach has been successfully applied with global and regional CTMs to identify spatial and temporal variations in O_3 sensitivity (Sillman, 1999).

In this paper, we computed the monthly tropospheric columns of NOx and key reactive VOC from the GC simulation to obtain the VOC/NOx ratio. This diagnostic allows us to understand the chemical regime across the tropics and examine its evolution over the past decades of O_3, providing insight into the relative roles of ANT and BB emissions in driving observed TOC trends.

3.6 Data analysis period

In the analysis section, the results are discussed across different periods, which are distinguished by their scope and scientific interest. The model-evaluation section, which includes the statistical analysis and the TOC trends from GC vs SOFRID-O_3, focuses on the 2008-2019 period. The GC model assessment was set for this period based on the quality and the availability of observational data for chemical species and to disregard the impacts of the COVID-19 pandemic (lockdowns in 2020). NO_2 and HCHO tropospheric columns from OMI are available from 2007 to 2021. Nevertheless, to include the 2021 year in the

https://doi.org/10.5194/egusphere-2026-1652
Preprint. Discussion started: 13 May 2026

model-evaluation, TROPOMI columns available from July 2018 to December 2021 must be used, as the column from OMI is less reliable after 2020. However, the columns derived from SOFRID-O_3 are available from 2008 to 2022, while SOFRID-CO are available from 2008 to 2020. In order to harmonise the analysis, we used the common timeframe of 2008–2019 based on the availability and the quality of the OMI/IASI-SOFRID datasets.

For the O_3 chemical regime section, the period 2007 to 2021 is considered for examining the correlation between the VOC/NOx ratio and TOC trends, and to evaluate whether the HCHO/NO_2 ratio can serve as a reliable proxy for the VOC/NOx ratio, as well as to enable comparison with recent studies using HCHO/NO_2 ratio. Furthermore, the 2007-2021 period is also examined in terms of the TOC trends under emission perturbations in order to provide further understanding of TOC trends in tropical regions and its connection to the chemical regime of O_3. Finally, the sensitivity test analysis, focusing on the role of BB and and ANT emissions, is performed over the 2017-2019 period to better quantify their impact on TOC in tropical regions.

4 Results and discussions

4.1 Assessment of the GC simulations with the satellite data constraint

This section examines the comparison of the NO_2 and HCHO tropospheric columns from GC simulations with the OMI observations, as well as the TOC and the CO total columns from SOFRID and the GC for the 2008-2019 period (sect 3.6).

The evaluation of GC simulations against satellite observations is performed on tropospheric columns (NO_2, HCO and O_3) and total columns (CO), without the application of averaging kernel matrix to the model columns due to the short atmospheric lifetimes of NO_2 and HCHO species, their concentrations are largely confined to the lower troposphere. In the model-evaluation, we use the simulated concentrations on the model grid, sampled at the times corresponding to the overpass of the UV-Vis sounders (OMI as 13h30 as LT) and the IASI (9h30 as LT). This allows us to choose the best inventory of ANT emissions and BB to best reproduce satellite observations with the models.

4.1.1 Bias analysis

Figure 2 displays the biases for the global and regional domains from Fig. 1. The blue and black curves in Fig. 2a represent results using the CEDS ANT emission inventory, while the red and magenta curves correspond to simulations using CAMS ANT emissions. Figure 2a shows that CAMS and CEDS produce similar biases for both global and oceanic regions (SPO, NAO, SAO and IO). For both inventories, the largest biases are located over Asian regions with the largest ANT emissions: China, SAs, and SEAs. The other important NO_2 emitters, Europe and TENAm are characterised by much lower biases meaning that the inventories better represent their emissions than those of Asian regions.

Over China and SAs the biases from the simulations with the CEDS inventory (REF1 and REF3) are significantly larger than those from simulations with the CAMS inventory (REF2 and REF4). The differences may stem from their methodology, spatial resolution, and data sources. The CEDS provides a long-term global emission record using generic proxies (e.g., population density, land use, etc.) and larger horizontal resolution ($0.5° \times 0.5°$), which may not capture local hotspots and/or seasonal

https://doi.org/10.5194/egusphere-2026-1652
Preprint. Discussion started: 13 May 2026

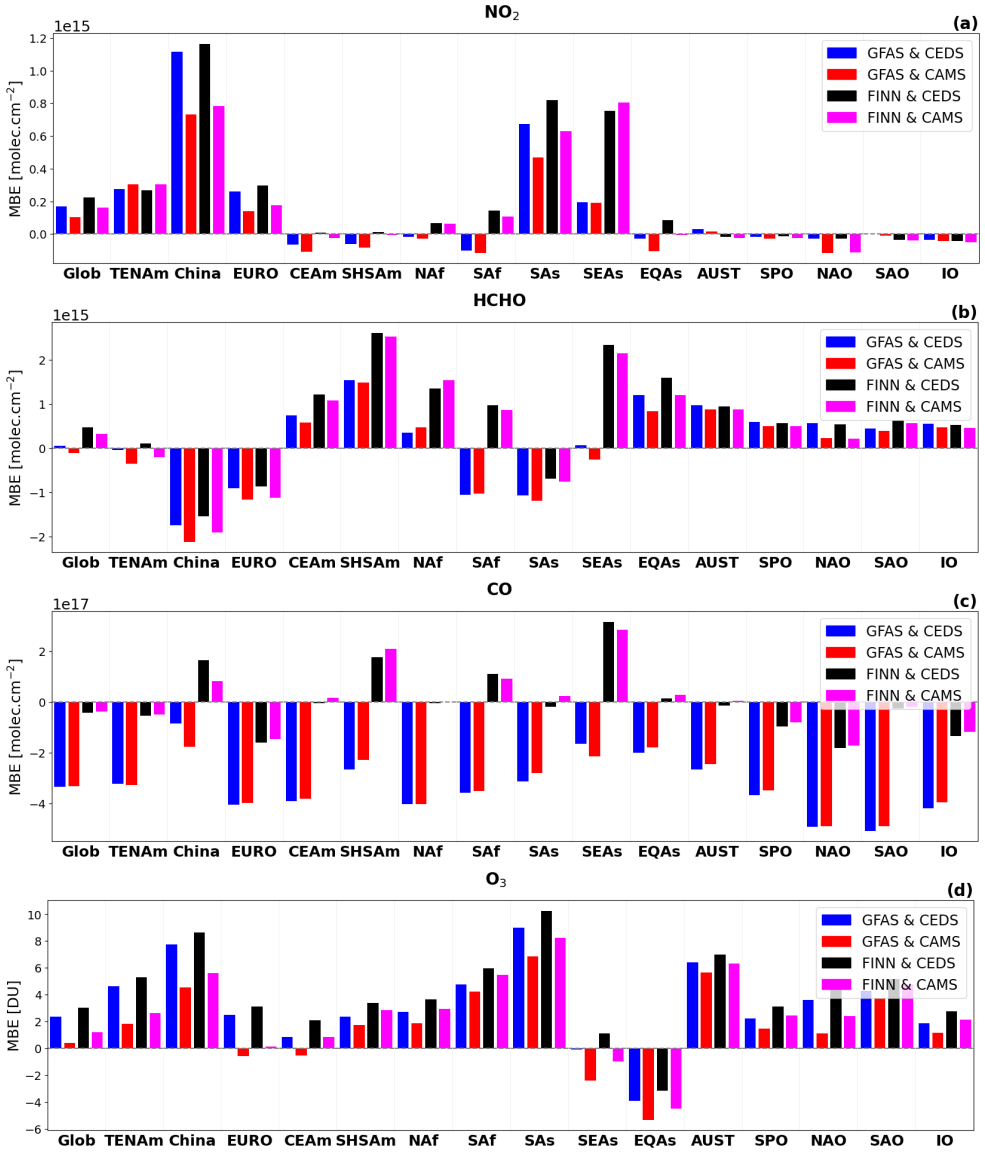

Figure 2. MBE [molec.cm^{-2}] for the GC relative to OMI/IASI column, over the 2008–2019 period for the global and the regional domains (a) NO_2, (b) HCHO, (c) total columns of CO and (d) tropospheric ozone column (TOC) (blue) REF1, (red) REF2, (black) REF3, (magenta) REF4.

variations (e.g, McDuffie et al., 2020; Chen et al., 2025), whereas CAMS incorporates observations and region-specific data with higher spatial and temporal resolution ($0.1° \times 0.1$ °), offering more accurate emissions in complex regions such as China and SAs (Soulie et al., 2024).

For the other regions, the differences between simulations with both ANT inventories concerning NO_2 is not significant.

https://doi.org/10.5194/egusphere-2026-1652
Preprint. Discussion started: 13 May 2026

Concerning BB emissions, the use of GFAS (blue REF1/red REF2) provides a slightly lower NO_2 bias in regions with intense BB activity (NAf and SAf) relative to FINN (black REF3/magenta REF4). GFAS also provides much lower biases over SEAs which is a region with large BB emissions. The GFAS inventory therefore provides better BB emissions of NO_2 emissions than FINN. This result is in agreement with Wiedinmyer et al. (2023) who have shown that the use of FINN tends to an overestimation of tropospheric NO_2 columns compared to other BB emission inventories in certain regions (e.g., SEAs, NAf, SAf). BB emission inventories differ due to methodological approaches. FINN uses satellite-detected active fires (MODIS hotspots) and fixed emission factors by vegetation type and fuel load at 1 km resolution, which can overestimate emissions by counting many small fires, especially in regions with widespread low-intensity burning (Wiedinmyer et al., 2011, 2023). However, GFAS uses Fire Radiative Power (FRP) from MODIS and scales emissions by fire intensity at $0.5° \times 0.5°$ resolution, producing lower totals and better capturing peatland fires that burn beneath the canopy and may be missed by hotspot-based inventories (Kaiser et al., 2012).

For HCHO (Fig. 2b), the use of GFAS generally results in lower biases with OMI than the use of FINN, in regions with intense BB emissions such as SHSAm, NAf and EQAs. GFAS and FINN show a similar order of magnitude of biases over oceanic regions such as SPO, NAO, SAO and IO. However, for the whole globe, the use of GFAS results in an almost null bias while FINN provides a significant positive bias.

The comparison between CO distributions from simulations with the CAMS and CEDS ANT emission inventories, (Fig. 2c, blue/black for CEDS vs. red/magenta for CAMS), does not reveal significant differences for the biases across all regions (oceanic, regional, and global) throughout the analysed period (2008–2019). The use of CAMS or CEDS has therefore a limited impact on modelled CO columns.

More significant discrepancies arise when comparing GFAS and FINN BB emission inventories, which exert a stronger impact on CO distributions. The results clearly indicate that the use of GFAS leads to a systematic underestimation of the CO columns compared to the use of FINN inventory. These results are not unexpected and have already been reported in studies using GC-model especially in the NH and for other chemistry transport models (Huijnen et al., 2019), which may be due to an overestimation of OH or missing CO emissions (e.g., Lin et al., 2024; Kopacz et al., 2010; Kim et al., 2022).

Figure 2d presents the distribution of the bias in the TOC (GC-IASI). Using the CEDS emission inventory (blue/black) leads to slightly lower overestimations than using CAMS (red/magenta) across all regions. Therefore, the analysis of the biases only is not sufficient to determine which emission inventory allows a more accurate representation of TOC.

4.1.2 Taylor Diagram analysis

In order to make the right choice of inventories, it is crucial to address the ability of the simulations to represent the spatiotemporal variations of the different target species. We present and discuss the Taylor diagrams (normalized) of the observations/simulation's comparisons (Fig. 3). The blue, red, black, and magenta colors in Fig. 3 represent the REF1, REF2, REF3, and REF4 GC simulations, respectively, for the global and regional domains from Fig. 1. For NO_2 tropospheric column, the variability with the using FINN as BB inventory (black/magenta colors in Fig. 3a) is largely overestimated, with standard deviation ratios larger than 1, particularly in regions impacted by BB such as SAs, CEAm, NAf, SAf, SHSAm, SEAs and EQAs (std

https://doi.org/10.5194/egusphere-2026-1652
Preprint. Discussion started: 13 May 2026

ratios > 4.2) where the ratios is upper to 1.5.

The R-values from FINN simulations are generally much lower than those obtained using the GFAS inventory, especially over some regions impacted by BB such as NAf, SHSAm, CEAm, SAs and SEAs (R-values around 0.2 with std.dev ratios > 4.2) and over oceanic regions (SPO, NAO, SAO and IO). GFAS is therefore more able to reproduce the NO_2 columns variations resulting from BB in both amplitudes (std.dev ratios) and phase (R-coefficient).

For HCHO (Fig. 3b), the simulations using GFAS generally exhibit higher correlation coefficients and standard deviation ratios closer to the reference point compared to those using FINN. In major BB regions such as SHSAm, GFAS yields R-values around 0.8 with a standard deviation ratio close to 1, while FINN gives lower correlations (R ∼0.6) and higher variability (std.dev ratio > 1), indicating an overestimation of the amplitude of the variability relative to OMI observations. At the global scale, GFAS simulations remain better correlated (R ∼0.6) with variability and RMSE ratios close to the reference, whereas FINN simulations show much lower correlation coefficients (R ∼0.4 and 0.7) and too large variability.

The overall analysis (MBE and Taylor diagram) indicates that the GFAS and CAMS emission inventories provide the best consistency with NO_2 observations from OMI. For HCHO, GFAS performs better than FINN, showing better variabilities and lower biases.

Figures 3c and 3d summarize the overall performance of the GC simulations for the total columns of CO and TOC over the 2008–2019 period, based on comparisons with SOFRID products. Simulations using FINN (black/magenta) as BB emissions exhibit too large CO variabilities with ratios from 1.2 to ∼3.5 (Fig. 3c). It is noteworthy that the combinations FINN/CEDS leads to the largest ratios meaning much too high variabilities relative. Simulations with GFAS (blue/red) provide better agreement with the observations with standard deviation ratios between ∼0.5 and 1.5. In addition, GFAS-based simulations generally display higher correlation coefficient ratio (R-values) across the four oceanic regions (SPO, NAO, SAO and IO), as well as at both global and regional scales (e.g., CEAm, EURO, TENAm) and result in lower centered RMSE ratios than FINN. These results indicate that GFAS emission inventories provide a better representation of BB emissions than FINN.

Figure 3d clearly shows that all the GC-simulations are clustered between ocean regions (SPO, NAO, SAO and IO), regions with high ANT emissions, and regions with high BB emissions. The weakest correlations with IASI-observations are found in the NAf and CEAm regions. However, R-values exceed 0.55 for all GC simulations over all regions, with standard deviation ratios ranging from 0.5 to 1.3. The agreement between GC and the SOFRID TOC is therefore good but the lack of differences between simulations show that TOC is not a good proxy for emission inventories selection.

GC-evaluation indicates that CAMS is the best ANT emission inventory based on the ability of the simulations to reproduce NO_2 with low biases and correct variabilities. Based on both biases for NO_2 and variabilities of the target species we also conclude that GFAS offers the representation of BB emissions most consistent with satellite observations. It is noteworthy that the CO underestimation with the GFAS inventory is general and therefore not related with the BB inventory itself but with a known underestimation of CO with the GC model. The CAMS-GFAS simulation (REF2) shows the best overall agreement with the satellite products.

For the following section, we focused on the REF2 GC simulation.

https://doi.org/10.5194/egusphere-2026-1652
Preprint. Discussion started: 13 May 2026

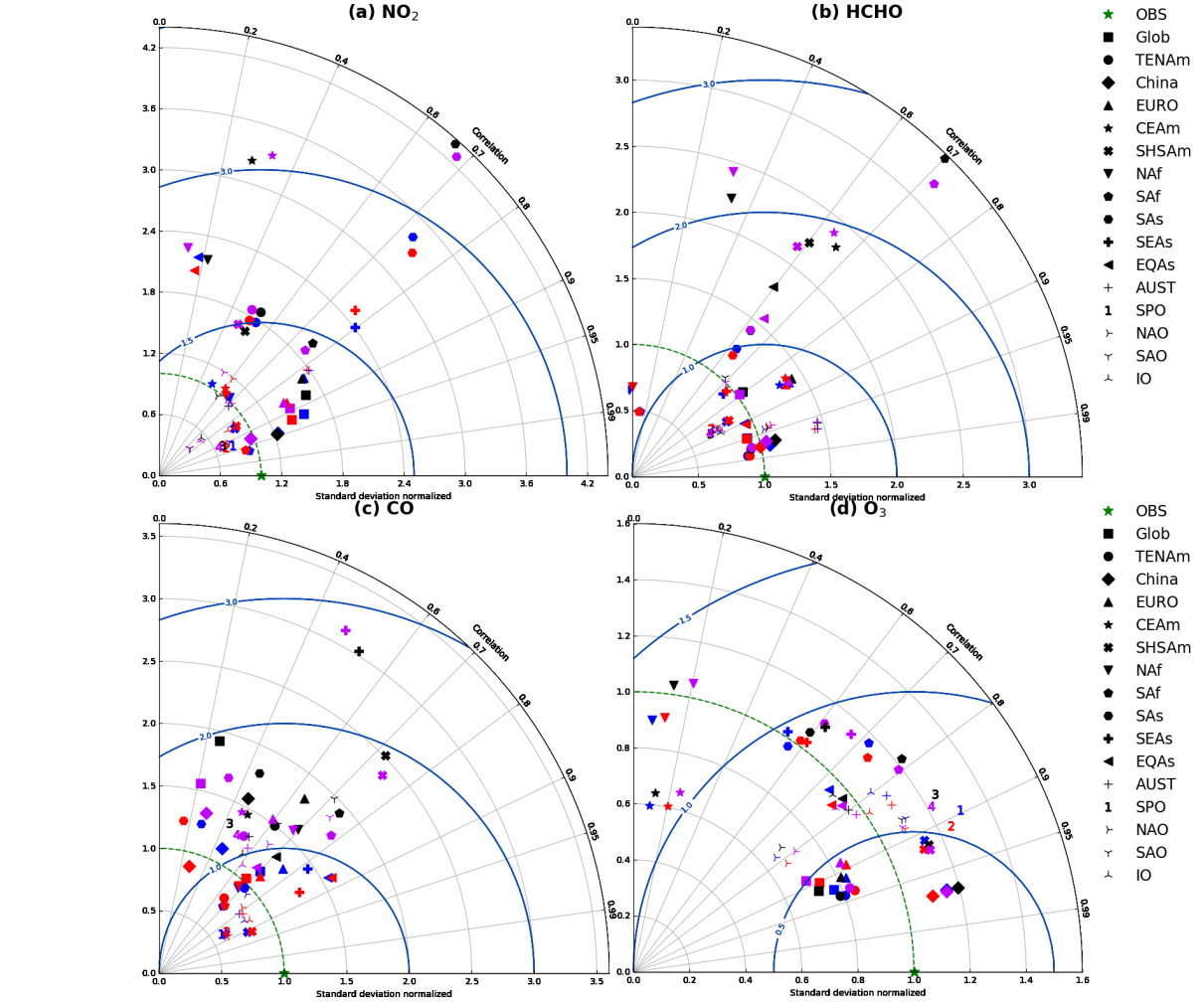

Figure 3. Taylor diagrams for the GC simulations comparisons versus OMI/SOFRID datasets over the 2008 - 2019 period for (a) NO_2, (b) HCHO (c) CO total columns and (d) TOC (blue) REF1, (red) REF2, (black) REF3, (magenta) REF4.

4.2 Global distributions of ozone and its precursors

Figure 4 displays a comparison of the 2008-2019 annual averages between satellite retrievals (OMI and IASI) and GC model simulation. According to the previous section (Sect. 4.1), we selected the "best" (REF2) simulation which uses a combination of CAMS ANT and GFAS BB emissions inventories, and defines the reference simulation (REF).

The distributions of the NO_2 tropospheric columns from OMI are largely consistent with the GC simulation (Figs. 4a, 4b) and the model captures very well the overall spatial distribution and the emission hotspots. However, the model tends to overestimate tropospheric NO_2 (Figs. 4b, A1a) over regions that are heavily industrialised and densely populated, such as China, TENAm, SAs and EURO regions. This discrepancy can be explained by clear-sky sampling bias in satellite NO_2, which

https://doi.org/10.5194/egusphere-2026-1652
Preprint. Discussion started: 13 May 2026

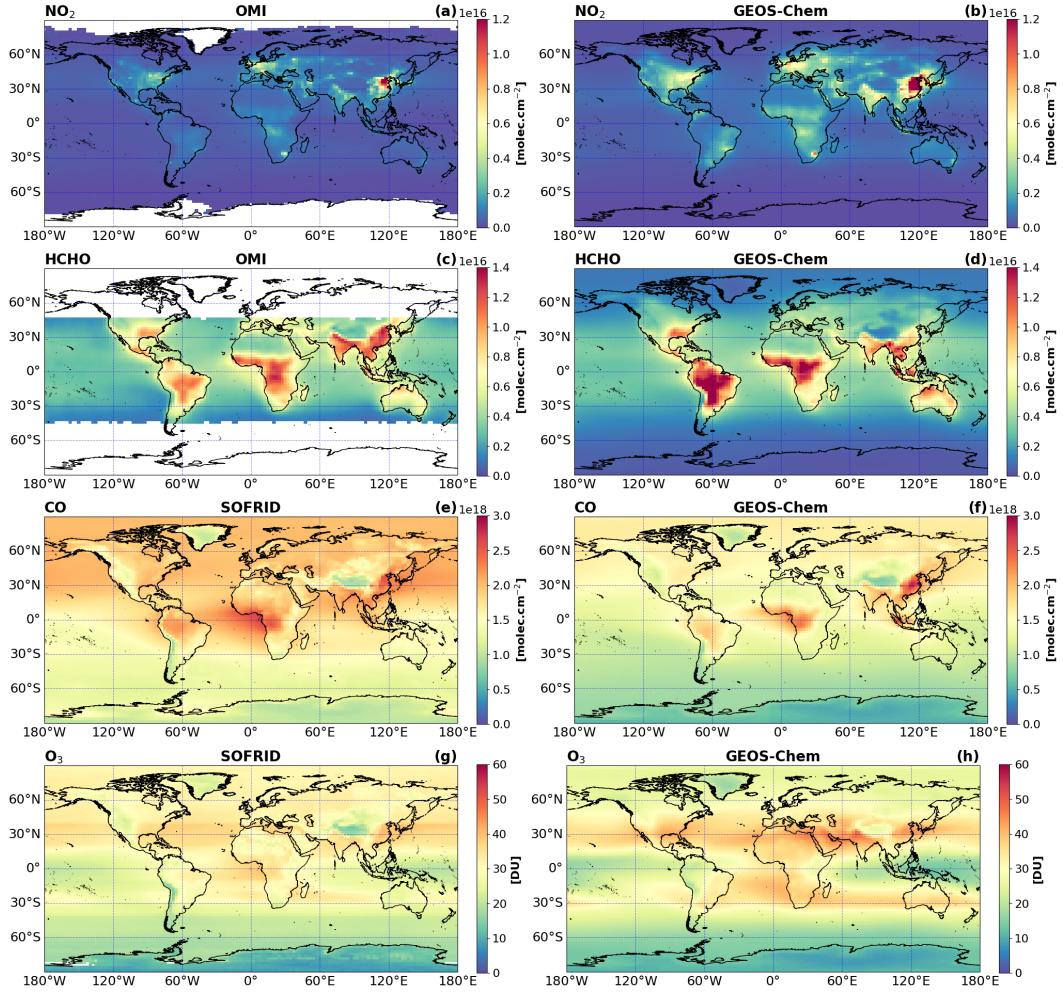

Figure 4. Tropospheric columns of NO_2 from (a) OMI (b) GC , HCHO (c) OMI (d) GC, CO total columns ($\mathrm{molec.cm^{-2}}$) from (e) SOFRID (f) GC and TOC (DU) from (g) SOFRID (h) GC averaged over the 2008-2019 period.

tend to underestimate tropospheric column values due to cloud screening, coarse spatial resolution and temporal sampling limitations; moreover, the lifetime of NO_2 is generally shorter in clear-sky conditions (e.g., Geddes et al., 2012; Boersma et al., 2016; Goldberg et al., 2017; Herman et al., 2019) compared to under all-sky in GC-modelled sampling.

HCHO tropospheric columns derived from the OMI and simulated by GC display similar features (Fig. 4c and 4d) with a similar order of magnitude (1E+16 $\mathrm{molec.cm^{-2}}$). The maxima, related to large biogenic (isoprene) emissions (e.g., Guenther et al., 2006, 2012; Lathière et al., 2006) are located over the same regions (Indochina peninsula, SHSAm, NAf).

In SAs and SEAs regions, the tropospheric HCHO column derived from OMI (Fig. 4c) are larger than the GC columns (Figs. 4d, A1b). This contrast may result from satellite retrieval bias. Clouds, aerosols and surface albedo can affect the measurement.

https://doi.org/10.5194/egusphere-2026-1652
Preprint. Discussion started: 13 May 2026

Over regions with high aerosols (SAs) or bright surfaces (SEAs), OMI may slightly overestimate HCHO, though usually not enough to explain very large differences (e.g., De Smedt et al., 2021; Zhang et al., 2025).

Furthermore, OMI HCHO data coverage is limited at high latitudes (north of 40°N and south of 40°S) because retrievals are filtered under snow- and ice-covered conditions (De Smedt et al., 2018), which is not allowed to make a complete comparison. The influence of BB emissions on HCHO is clearly overestimated by GC, particularly in the SHSAm, NAf and SAf regions (sec. 4.1 and Fig. 2). In these areas, GC tends to overestimate HCHO columns, reflecting uncertainties in the GFAS BB emission inventories. Additionally, the chemical conversion of non-methane volatile organic compounds (NMVOCs) and isoprene to HCHO can produce excess concentrations if oxidation or loss processes are oversimplified (e.g., Sun et al., 2025). Further discrepancies may arise from limitations in the model's representation of transport and deposition processes (e.g. Wang et al., 2025).

Figure 4e shows that the general pattern of the CO annual distributions from SOFRID is correctly reproduced by the REF2 simulation (Fig. 4f). Nevertheless, GC clearly underestimates the CO total columns (Fig. A1c) globally in agreement with what has been previously shown in the evaluation of the simulations.

The distribution of TOC from the REF2 simulation agrees well with the SOFRID retrievals (Figs. 4g and 4h). However, it displays bands of overestimated TOC at the tropical outer boundaries (30°S and 30°N, Fig. A1d). This discrepancy is unlikely to reflect excessive stratospheric influence, as GC calculates TOC using MERRA-2 meteorology and a dynamically defined tropopause. Instead, this discrepancy is likely derived from methodological differences in TOC definition and vertical sensitivity: SOFRID derives TOC from vertically smoothed O_3 retrievals, constrained by a priori climatological profiles linked to the WMO tropopause, while GC integrates O_3 up to a dynamic tropopause defined by the model.

Furthermore, the model overestimates values at the edge of the tropics (Fig. 4h), which correspond to long-distance transport, particularly of fire plumes in the SH.

4.3 Tropospheric ozone trends

4.3.1 Regional linear trend

Figure 5 presents a time evolution of TOC between 2008 and 2019 for global and different regional domains, as derived from SOFRID (green) and from GC simulations (red). As expected, extratropical regions (China, SAs, AUST) exhibit the clearest annual cycles while regions close to the equator (EQAs, CEAm, NAf) display less seasonal variability. TOC from SOFRID and GC (Fig. 5a) display similar seasonal variabilities, but GC produces a positive global trend of +0.182 $\mathrm{DU\ yr^{-1}}$ when SOFRID provides a much lower trend (+0.035 $\mathrm{DU\ yr^{-1}}$). The positive trend in GC is consistent with rising ANT emissions of O_3 precursors in SAs and SEAs regions, from CAMS emission inventories.

At the regional scale (SEAs, EQAs, CEAm, NAf and SAf), TOC trends are lower and close to zero, and the agreement between GC and SOFRID is more uncertain, with significant differences in the magnitude of the seasonal cycle. In the SH, GC and SOFRID display marked seasonal cycles, but overall the GC trends are more positive than SOFRID. In general, TOC trends from GC simulations systematically overestimate the TOC trends from SOFRID (Fig. 5), with significant regional variations.

https://doi.org/10.5194/egusphere-2026-1652
Preprint. Discussion started: 13 May 2026

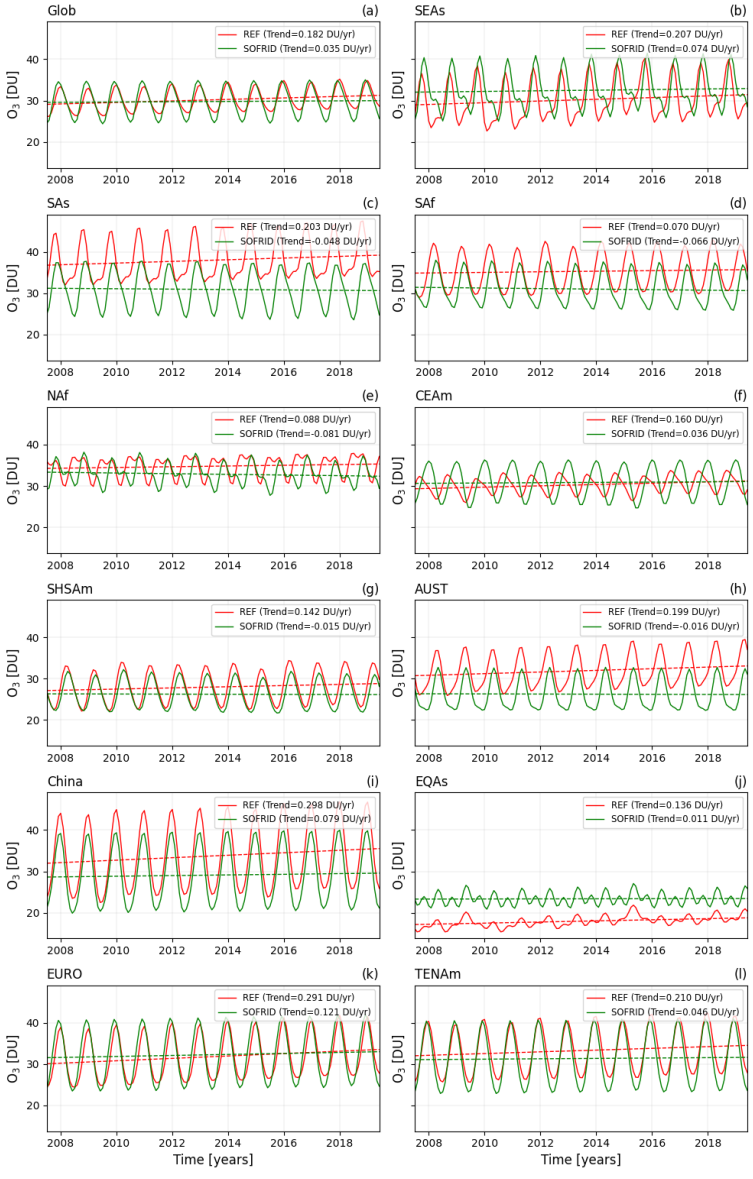

Figure 5. Time series of the TOC (DU) between 2008 and 2019, as derived from SOFRID (green color) and REF simulation (red color). All dashed lines correspond to the linear trends derived from the simplified model (equation 1) for global (a) and regional (b) to (l) domains.

GC simulation highlights strong regional differences in the evolution of TOC between 2008 and 2019. The most significant positive trends appear in the mid-latitudes of the NH, especially in China, Europe, TENAm, SEAs and SAs regions (Figs. 5i, 5k, 5l, 5b and 5c), where the increase is greater than 0.2 DU yr^{-1} due mainly to the increasing of the ANT emission in these periods (Parrish et al., 2021; Bowman et al., 2022) and is associated with a strong seasonal variability. In contrast, tropical Africa regions (NAf and SAf) show weaker trends and less pronounced seasonal cycles, reflecting variability dominated by

https://doi.org/10.5194/egusphere-2026-1652
Preprint. Discussion started: 13 May 2026

tropical dynamics.

The CEAm (Fig. 5f) and the SH regions, including SHSAm, EQAs and AUST (Figs. 5g, 5j and 5h), shows moderate positive trends, with strong variations but less significant compared to the NH regions. On a global scale (Fig. 5a), the GC trend is therefore mainly the product of the contribution of mid-latitude regions, while the tropical regions contribute less to the increase in the TOC.

The IASI instrument, operating in the thermal infrared, is more sensitive to ozone concentrations in the mid-and upper troposphere and less near the surface where most of the TOC increase related to ANT activities occurs. A study from the TOAR-I project has shown important discrepancies between UV-Vis and TIR sensors for the TOC trends (Gaudel et al., 2018). TOC retrieved from UV-Vis sensors provided positive global trends while retrievals from TIR sensors resulted in negative (FORLI algorithm) or insignificant trends (SOFRID). It has to be noted that UV-Vis sensors are more sensitive to O_3 even at higher altitudes (UTLS) than the IR sensors which cannot explain the trends discrepancies. Comparing three IASI retrievals, Pope et al. (2024) confirm the absence of significant TOC trends with this sensor such as shown with SOFRID in Gaudel et al. (2018). The reason for the discrepancy between UV-Vis and TIR sensors was not understood at the time of Gaudel et al. (2018) but is confirmed in the TOAR-II satellite assessment report (Hubert et al., in review).

4.3.2 Global distribution of TOC trend

We present in Fig. 6 the TOC trends simulated by GC over 2007–2021 period (% decade^{-1}), with statistically significant values ($p \leq 0.05$) highlighted by an asterisk symbol. Figure 6 clearly shows that the spatial distribution of the trends reveals several pronounced and regionally coherent features.

Figure 6 displays the strongest positive TOC trends occurring over SEAs and the wider EQAs regions, where values exceed +8%. These very large increases are consistent with rapid regional growth in ANT emissions (NOx, CO, VOCs), and intense BB activity, which together provide a highly favourable chemical environment for O_3 formation.

Similar patterns of enhanced O_3 growth over SAs and part of the South China sea have been documented in satellite analyses and merged observations extending back to 1979, which reported net increases of roughly 6DU to 7DU over East and SAs equivalent to about +15% to 20 % of typical background levels (Ziemke et al., 2019). Recent multi-platform observational syntheses also confirm an upward trend in lower and mid-tropospheric O_3 throughout SEAs and the tropical western Pacific, driven by both emissions and large-scale transport variability (e.g., Gaudel et al., 2024; Thompson et al., 2025).

We also observe that the pattern of the TOC trend (Fig. 6) is consistent with the findings of Hubert et al. (in review) in their TOC trend results over the 2005-2022 period. Hubert et al. (in review) is based on a robust product combining 10 satellite retrievals from UV-Vis and IR sensors. They found the same positive TOC trend in SEAs and EQAs regions similar to GC (Fig. 6). However, the results presented in Fig. 6 are much greater (-15% to +15% decade^{-1}) than those found by Hubert et al. (in review) which are between -6% and +6% decade^{-1}. This discrepancy may be explained by the different years of comparison (2005-2022 vs 2007-2021) and the horizontal resolution of GC vs. the combination of several satellites that were used. By contrast, negative trends in TOC (Fig. 6), reaching -5% to -10%, are evident in the northern and southern tropical Pacific, as well as in equatorial Africa. However, the middle latitudes of the SH display either a weak positive trend (Fig. 6),

https://doi.org/10.5194/egusphere-2026-1652
Preprint. Discussion started: 13 May 2026

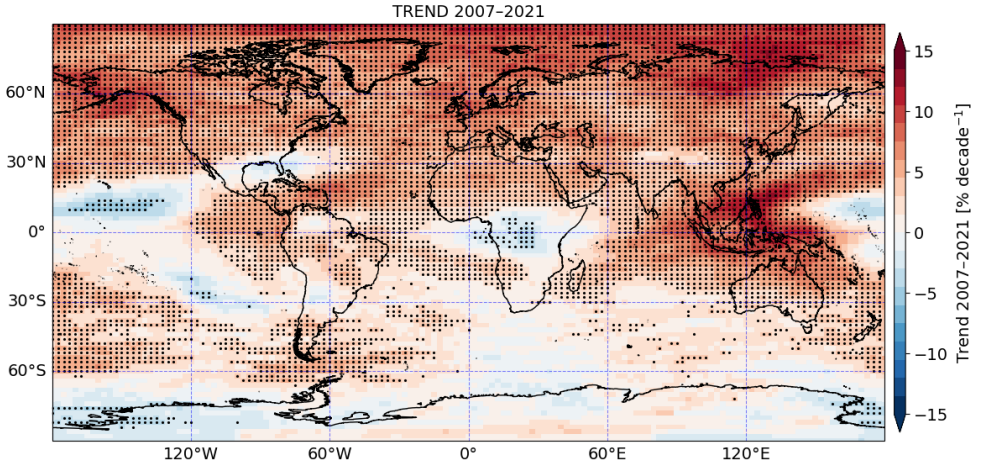

Figure 6. Global trends of the TOC (% decade^{-1}) over the 2007 - 2021 period, as derived from GEOS-Chem simulation (REF). The asterisks symbol mark grid cells where trends are statistically significant at $p \leq 0.05$

or nonsignificant trends (close to zero or slightly negative) in good agreement with many satellite datasets and the combined satellite product presented in Hubert et al. (in review) especially in the Eastern South America region, suggesting relatively stable O_3 levels. This stability reflects lower precursor emissions, limited industrial development compared to the NH, and a stronger oceanic influence.

In addition to the regional hotspots, Fig. 6 shows that large positive trends (+5% to +10%) extend across the mid-latitudes of the NH, particularly in East Asia, Europe, the Middle East and the TENAm regions and these trends are consistent within the results obtained by Hubert et al. (in review). Recent studies show that the positive trends in TOC observed in the mid-latitudes of the NH (30°N - 60°N) result from a combination by O_3 precursor emissions and long-range transport of polluted air masses, as well as by intrusions of stratospheric O_3 into the troposphere (e.g., Elshorbany et al., 2024; Li et al., 2024).

A significant positive trend (exceeding +10% decade^{-1}) occurred at latitudes above 80°N (Fig. 6). These increases may result by the transport of O_3-rich air masses from mid-latitudes towards the polar regions, as well as increased exchange between the stratosphere and troposphere in a warming climate, which have also been identified in previous analyses of satellite trends (Ziemke et al., 2019). Seguel et al. (2025) have shown that TOC is higher in the NH compared to the SH, leading mainly to this TOC trend in mid-latitudes and at the North Polar regions.

Similar increases at mid-latitudes have been reported in the TOAR-II global assessments and long-term satellite records, which highlight that background O_3 over the NH remains high relative to the end of the 20th century (e.g., Wang et al., 2022; Gaudel et al., 2024; Van Malderen et al., 2025).

The consistency between the spatial patterns identified here and those reported by recent studies based on satellite products (e.g., Elshorbany et al., 2024; Hubert et al., in review), indicates that the results from our REF-simulation (Fig. 6) are robust and representative in general of the larger trend in TOC over the past decade. Overall, this analysis reinforces the current

https://doi.org/10.5194/egusphere-2026-1652
Preprint. Discussion started: 13 May 2026

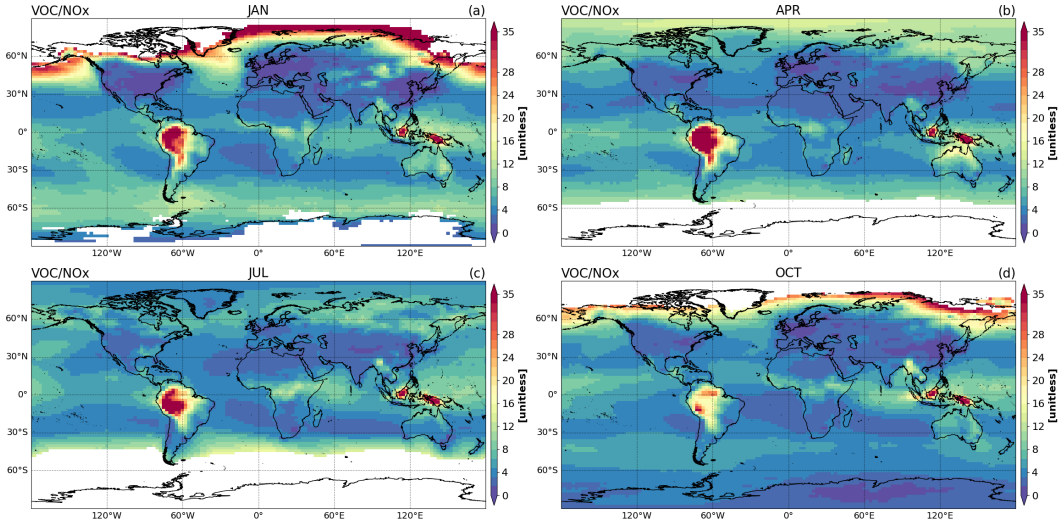

Figure 7. Monthly averages of VOC/NOx in the tropospheric column derived from REF simulation for the period 2007-2021. Panel (a) January, (b) April, (c) July, and (d) October. The ratio is computed by taking account of the NOx tropospheric column above 1E+14 $\mathrm{molec.cm^{-2}}$. The "white" colour range, especially for January/October in the NH (above 60°N) and in April/July in the SH beyond 60°S is mainly due to the lower tropospheric NOx column. Similarly, the high values of the ratio near the North Polar reflect the low NOx-levels approximately $\sim$1E+14 $\mathrm{molec.cm^{-2}}$. The production of NOx species by photochemical reactions is slightly reduced.

scientific consensus about localised positive TOC trends, reflecting mainly a combination of ANT and BB emissions, long-range transport, and climate variability especially in tropical regions.

Moreover, West and Fiore (2005) underline that the increase in CH_4 emissions contributes to raising the background level of O_3 on a hemispheric scale, reinforcing this positive trend despite emission control measures (NOx and NMVOCs) in certain regions. The control of emissions in certain regions could also lead to an increase in O_3 due to a more favourable chemical regime. An additional reason may be the transport of O_3 from other regions. Therefore, we focus in the following section on the possible impact of chemical regime (e.g., Sillman, 1999) changes on the evolution of O_3 in order to better understand this increase in TOC trend derived from the GC simulations described above.

4.4 O_3 chemical regime and sensitivity results

4.4.1 VOC/NOx ratio

We computed the total VOC to NOx ratio derived from REF-simulation to better understand the O_3 chemical regime. We present in Fig. 7 the spatial distribution of the average VOC/NOx ratio derived from the REF simulation for the months of January, April, July and October averaged over the 2007-2021 period, highlighting the marked seasonal and regional contrasts in O_3 chemical regimes in tropical regions.

The high ratio values (VOC/NOx $>$ 8) are consistently observed across equatorial regions dominated by strong biogenic VOC

https://doi.org/10.5194/egusphere-2026-1652
Preprint. Discussion started: 13 May 2026

emissions, particularly in SHSAm and EQAs regions. In January and April (Figs. 7a and 7b), the tropical maxima is especially intense, reflecting strong isoprene emissions sustained by warm and humid conditions. In July (Fig. 7c), the shift of the Intertropical Convergence Zone (ITCZ) enhances the ratio over central and northern southern America, equatorial Africa and EQAs, while the southern Amazon shows a slight reduction linked to the transition toward the dry season. By October (Fig. 7d), ratios remain elevated over SHSAm and EQAs where both biogenic fluxes and BB activities contribute while a moderate decline is detected over SHSAm region toward the end of the dry season. These regions are characterized by the regime of NOx-limited, that means the abundance of the total VOC compared to the NOx. This could be explained by the abundance of VOCs emission especially from the isoprene species in these regions; the production of the O_3 is therefore controlled by the VOC species abundance but in presence of the NOx. In contrast, the mid-latitude regions display systematically lower ratios (VOC/NOx < 4) and/or transition regime, in line with dominant ANT NOx emissions and the associated VOC-limited chemical regime typical of industrialized regions in TENAm, Europe, SAs, SEAs, and part of China. Hence, the moderate TOC trend shown in SHSAm and EQAs regions (Figs. 5g and 5j) is associated with a NOx-limited regime, while the strong TOC trend is generally associated with a VOC-limited regime. This suggests that the evolution of TOC in mid-latitude regions is governed by NOx-ANT emissions, while the TOC trend observed in tropical regions (SHSAm, EQAs) is controlled by the VOC-emissions that characterise rural regions.

Figure 8 displays the regional average time series of the VOC/NOx ratio for several regions (Fig. 1) over the 2007-2021 period. The temporal evolution highlights contrasting behaviours between regions that have implemented emission control policies and those undergoing rapid urbanisation, such as China. We have already described in section 3.5 the classification of two chemical regimes related to the VOC/NOx value used to define the production of O_3.

The Europe and TENAm regions (Fig. 8a) exhibit a continuous increase and China a decrease of the VOC/NOx ratio (Fig 8a). In the Europe region, we note in Fig. 8a that there is significant variability compared to the TENAm region and China from 2010 onwards. This is due to the decrease in NOx concentrations in Europe (Fig. A3a), where the shift of major NOx sources from power generation to industrial and transportation sectors has coincided with noticeable diminishing effects in emission controls. Although ANT NOx emissions in the US have been declining since 2010 (e.g., EU, 2003; Crippa et al., 2016), the VOC/NOx ratio remains low associated with the VOC-limited chemical or transition regime. In contrast, Fig. 8d (EQAs and SHSAm) clearly shows that the VOC/NOx ratio is higher which is associated by the NOx-limited chemical regime which is due to the abundance of VOCs mainly from the isoprene emission and/or photochemistry efficiency.

For regions with high ANT activity such as TENAm and Europe (transition or VOC-limited regime), the TOC trend derived from GC is positive (Figs. 5k and 5l) and is generally a significant trend in relation with VOC/NOx trend positive (Fig. 8a). This explains that the significant TOC trend observed in these regions is governed by the NOx emission. Especially the control emissions in these regions influenced the change of chemical regime of O_3 production. However, in the China region, the TOC trend (Fig. 5i) increases rapidly while the VOC/NOx ratio trend (Fig. 8a) decreases (and associated with VOC-limited regime) , mainly, explained by the rapid decline of NOx tropospheric columns since 2010 (Fig. A3b).

The SAs and SEAs regions have a high TOC trend (Figs. 5b, 5c) and are also associated with a transition and/or VOC-limited regime (Fig. 8b) and negative VOC/NOx ratio trends. These results in regions associated with VOC-limited regimes do not

https://doi.org/10.5194/egusphere-2026-1652
Preprint. Discussion started: 13 May 2026

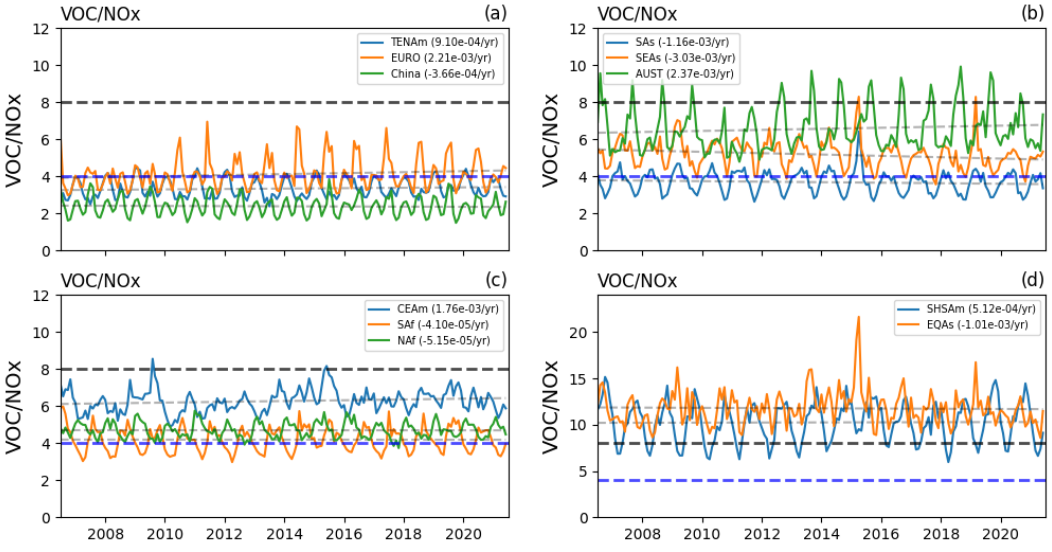

Figure 8. Time series of the VOC/NOx ratio between 2007 and 2021, as derived from GC for the TENAm, EURO and China regions (a), SAs, SEAs and AUST regions (b), CEAm, SAf and NAf regions (c) and for SHSAm and EQAs regions (d). The grey dashed lines correspond to their respective linear trends. Black dashed line represents the threshold VOC/NOx = 8 and the blue dashed-line for VOC/NOx = 4.

allow us to conclude that the increasing TOC trend in these regions is explained by the VOC/NOx ratio trends. However, the rapid reduction in NOx decreases O_3 titration and enhances photochemical efficiency, leading to an increase in TOC (Sillman, 1999; Duncan et al., 2010) despite the decrease in VOC/NOx ratios.

Similarly, there is also a discrepancy between the SHSAm and EQAs regions, which both show moderate TOC trends (Figs. 5g and 5j) and chemical regimes controlled by NOx (Fig. 8d, NOx-limited). The higher ratio is mainly from BB and biogenics VOCs emissions. In the SHSAm region, TOC trends (Fig. 5g) and VOC/NOx ratios trend (Fig. 8d) are both positive; nevertheless, moderate TOC trend occured in the EQAs region (Fig. 5j) are associated with a negative trend of VOC/NOx ratio (Fig. 8d). As presented in the regions with VOC-limited or transition regime (TENAm, Europe, China, SAs and SEAs regions) discussed previously, the increase of TOC trend in the region with NOx-limited regimes (SHSAm and EQAs regions) is not always related to the VOC/NOx ratio positive trend. Despite the non-statistically significant results for the VOC/NOx ratio trend, the increase of TOC trend is not directly related to the VOC/NOx trend. The suspected reasons are that the O_3 chemistry is non-linear and as presented in the literature, meteorological conditions may play an important role in affecting the O_3 production since O_3 is a secondary species.

Although the analysis presented in this study was based on total VOCs and NOx, unlike previous published analyses that use specific indicators (HCHO and NO_2) to determine the chemical regime of O_3 given the limitations of observations. Overall, our results concerning the VOC/NOx ratio are generally consistent with those already reported in the literature regarding the HCHO/NO_2 ratio (e.g., Elshorbany et al., 2024; Tian et al., 2025). Elshorbany et al. (2024) report persistent high HCHO/NO_2 ratios over the tropical regions, highlighting strong NOx-limited while lower HCHO/NO_2 ratios observed in certain regions of

https://doi.org/10.5194/egusphere-2026-1652
Preprint. Discussion started: 13 May 2026

the NH regions (Western Europe, Northern Asia, Northeastern of US) from 2005-2019 period. Similar conclusions are drawn from the TOAR-II assessments (Gaudel et al., 2024; Van Malderen et al., 2025) and GC/OMI model evaluations (Zhu et al., 2016; Wang et al., 2022), all of which emphasize the stability of these tropical maxima and the contrasting regimes in ANT hotspots. These features which are mainly based on multi-sensor analyses based on OMI and TROPOMI retrievals and on model are consistent with our findings in terms of the chemical regime of O_3 (VOC/NOx ratio).

The hemispheric contrasts reported by Tian et al. (2025) show positive trends in developed regions (TENAm, EURO) and negative trends in rapidly industrialising region (China), while Elshorbany et al. (2024) highlighted the persistent influence of NOx emissions on O_3 precursor ratios in the tropical regions. Previous studies (e.g., Duncan et al., 2010; Souri et al., 2020) has shown that the $HCHO/NO_2$ ratio effectively captures changes in photochemical regimes in response to ANT emission controls. From 2007 to 2021, VOC/NOx ratio trends indicate that regions with declining NOx emissions are shifting towards VOC-limited regimes, while the EQAs and SHSAm regions remain mostly NOx-limited. These findings confirm the agreement between the GC model (VOC/NOx) and satellite diagnostics ($HCHO/NO_2$) and highlight the importance of further supporting efforts to control VOC and NOx emissions in order to reduce TOC on a global scale.

In addition to the consistency of our results with the literature on the $HCHO/NO_2$ studies, the VOC/NOx ratio presented in Fig. 7 is in good agreement with its proxy ($HCHO/NO_2$ ratio, Fig. A2) derived from GC for the same period 2007 to 2021. We find the similar structure and pattern as well as the chemical regimes of O_3 production associated with NOx-limited (SHSAm and EQAs), and VOC-limited or transitions mostly in the NH mid-latitude region.

Even though there is no clear link between the increase in TOC and the chemical regime of O_3 production, there is interest to better understand the role of emission from BB and ANT on TOC.

4.4.2 Role of anthropogenic and biomass-burning emissions

We analyse in this section the results from two sensitivity simulations performed in order to quantify the impact of tropical emissions on TOC on the regional and global scales. The global distribution of seasonal mean differences in TOC (DU) between the REF simulation with the two sensitivity tests: ANT_Fix and BB_Fix (see Table 2 for description) over the 2017-2019 period are displayed in Fig. 9.

The REF-BB_Fix (left panels) shows a consistent pattern of negative TOC anomalies in the major tropical regions affected by BB emissions, with significant reductions in equatorial Africa and SHSAm regions. Regarding Fig. 9, the negative anomalies are mainly stronger during the SON (Fig. 9g) and DJF (Fig. 9a), coinciding with the dominant burning seasons in the African and in the SHSAm regions. The spatial signature of these anomalies is mostly limited to known fire hotspots, highlighting the regional and seasonal role of the BB in tropical O_3 formation. The relatively weak anomalies observed during MAM season (Fig. 9c) corresponds to lower intensity of burning, while the JJA season (Fig. 9e) shows moderate TOC difference but nevertheless significant anomalies in regions with high burning activity especially in SHSAm and SAf regions.

Previous studies reveal that anomalies in TOC caused by burning in tropical regions exhibit a marked seasonal cycle. The SON season has the most significant negative anomalies in tropical regions in SHSAm and Africa, as well as in northern of AUST and EQAs regions, reflecting the maximum BB emissions from dry-season under favourable photochemical conditions (e.g.,

https://doi.org/10.5194/egusphere-2026-1652
Preprint. Discussion started: 13 May 2026

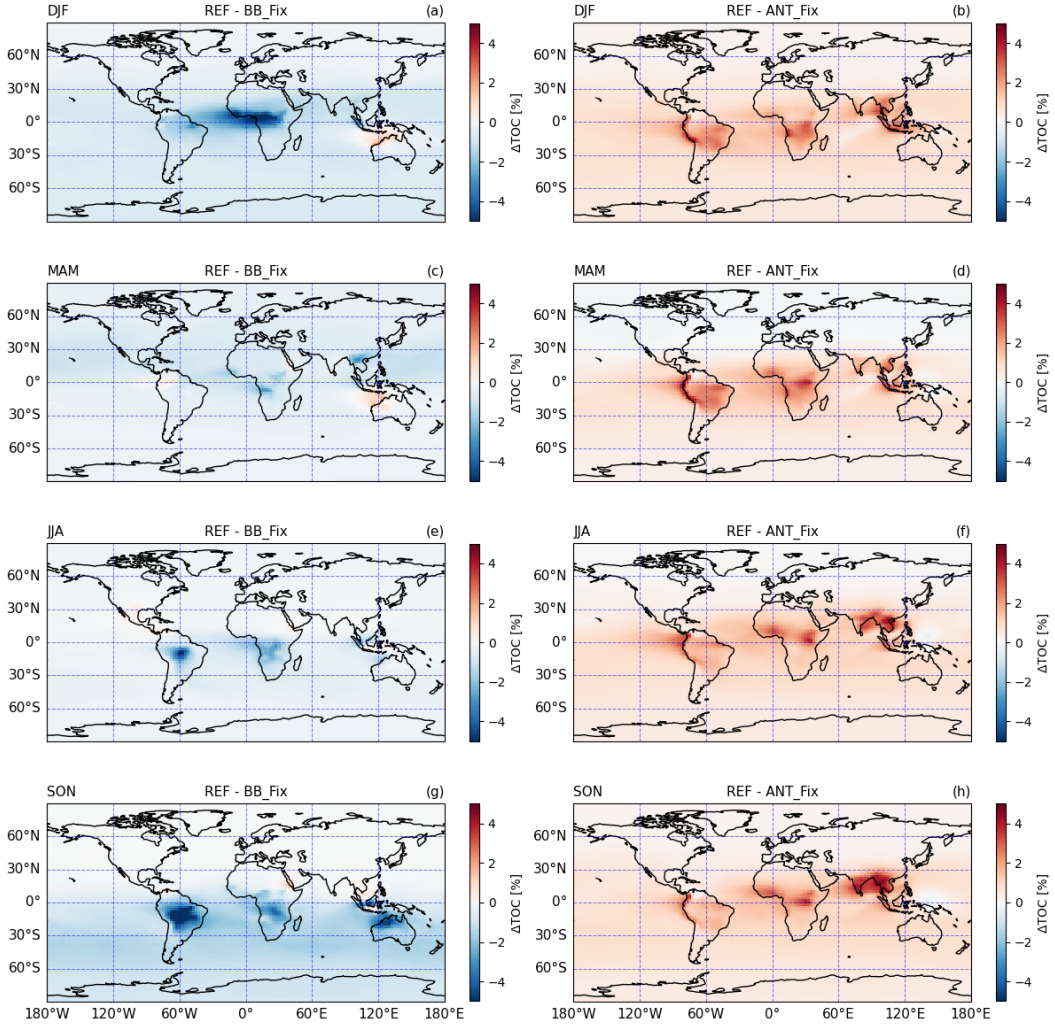

Figure 9. Seasonal differences in TOC [%] between the REF simulation and BB_Fix ((a), (c), (e), (g)) and ANT_Fix ((b), (d), (f), (h)) simulations tests over the 2017-2019 period.

Ziemke et al., 2009). Significant anomalies are observed during the DJF season (Fig. 9a), which probably result from a combination of several factors: regional burning intensity in equatorial Africa, part of Australia and of SHSAm regions, interannual variability such as ENSO, and long-range transport from mid-latitude burning, which especially affects the free troposphere (e.g., Young et al., 2018). The JJA season shows moderate anomalies in TOC over SHSAm, SAf, and EQAs regions, indicating that burning activity and transport processes during this season contribute to O_3 enhancement, although in general to a less significant extent than during the SON season. In contrast, the MAM season shows relatively low anomalies in the tropics, consistent with a transition season characteristic of reduced burning activity and less photochemical production.

The results from REF-ANT_Fix (Fig. 9, right panels) shows a persistent and widespread seasonal pattern of positive TOC

https://doi.org/10.5194/egusphere-2026-1652
Preprint. Discussion started: 13 May 2026

anomalies, generally extending over much of the tropical belt. Figure 9 (right panels) clearly shows that TOC increases are particularly strong in SAs and SEAs regions during JJA and SON seasons. Moderate anomalies are observed in equatorial Africa and SHSAm regions for all four seasons. One of the reasons for the increase of TOC may be due to the increase in ANT emissions and eventually the increase of tropospheric NOx columns (Fig. A3c). Since the photochemistry is abundant in tropical and equatorial regions, then O_3 production from the NO_2 photolysis reaction is also significant, that is the way the EQAs region shows a moderate increase in TOC, in particular during DJF and MAM seasons. The spatial consistency and persistence of these positive anomalies reflect the broader influence of ANT emissions. The results suggest that ANT emission trends lead to a significant increase in TOC at the regional scale in tropical regions between 2017 and 2019, while the decrease in BB emissions had a balancing effect. The combined results of the REF-BB_Fix and REF-ANT_Fix clearly reveal that the ANT emissions dominate the positive TOC trend, while BB decreases contribute to offsetting reductions in O_3 in key regions where burn intensity is highest.

Several studies have investigated long-term O_3 variability and its drivers, highlighting the roles of ANT, BB emissions and circulation patterns (e.g., Zhang et al., 2016; Gaudel et al., 2018; Jaffe et al., 2018; Bourgeois et al., 2021). However, many of these analyses relied on global perturbation experiments or broad regional assessments. This present study contributes to our understanding in several key ways. Firstly, by fixing emissions within the tropics (25°N-25°S), we directly quantify how tropical emission trends alone influence TOC evolution, providing a more targeted attribution than global-scale sensitivity tests. Secondly, we clearly separate opposing O_3 trends : declining O_3 due to reduced BB versus increasing O_3 driven by rising ANT emissions, highlighting a dual trend decomposition rarely presented with such clarity. Finally, by explicitly showing how BB and ANT emissions differently affect TOC across seasons, our results from the GC model help reconcile the contrast of TOC tropical trends observed by both satellites (OMI/TROPOMI) and chemistry transport models (CTMs). These contributions provide a high-resolution framework for understanding how TOC in tropical regions responds to changes in emissions, providing insights that may have been considered in previous global or regional studies.

The correlation with the VOC/NOx (Fig. 7) and HCHO/NO_2 (Fig. A2) also provides a basis for understanding O_3 sensitivity tests. Regions with high values of ratios (NOx-limited regime) in both diagnostics of O_3 chemical regime show a negative TOC response in REF-BB_Fix (Fig. 9, left panels) compared to REF-ANT_Fix (Fig. 9, right panels) results, demonstrating that long-term TOC trends in these regions are mainly controlled by VOCs availability rather than NOx variability. In contrast, the regions with lower ratios (Figs. 7, 8 and A2) show a significant positive TOC response to fixed ANT emissions, consistent with VOC-limited or transition regime where NOx reductions only are less effective. Overall, the agreement between these two chemistry regime indicators and their correspondence with sensitivity tests enhances the conclusion that spatial differences in chemical regime might play a key role in tropical regions TOC trends.

4.4.3 Global and regional TOC trends under emission perturbations

To quantify long-term changes in TOC under different emission perturbation scenarios, we computed the TOC trends for REF, BB_Fix and ANT_Fix simulations over the period 2007-2021 with respect to the simplified equation 1. Monthly mean TOC values were first averaged over predefined domains (Fig. 1). Table 3 summarises the TOC trends from GC between 2007 and

https://doi.org/10.5194/egusphere-2026-1652
Preprint. Discussion started: 13 May 2026

Table 3. TOC trends derived from the simplified model (equation 1) for 2007–2021 ($DU\ yr^{-1}$)

Regions	REF	ANT_Fix	BB_Fix	REF - ANT_Fix	REF - BB_Fix
Glob	0.164	0.146	0.182	0.018	-0.017
SEAs	0.178	0.128	0.196	0.050	-0.018
SAs	0.142	0.102	0.155	0.040	-0.013
SAf	0.012	-0.028	0.057	0.040	-0.044
NAf	0.094	0.050	0.124	0.044	-0.031
CEAm	0.111	0.107	0.122	0.005	-0.010
SHSAm	0.091	0.066	0.122	0.025	-0.031
AUST	0.122	0.100	0.154	0.022	-0.032
China	0.212	0.201	0.221	0.012	-0.008
EQAs	0.136	0.112	0.150	0.024	-0.014
EURO	0.214	0.208	0.221	0.005	-0.007
TENAm	0.155	0.148	0.163	0.006	-0.008

2021 for the reference simulation (REF) and the two sensitivity simulations ANT_Fix and BB_Fix.

At the global scale (Glob), the REF simulation shows a positive trend of +0.164 $DU\ yr^{-1}$, which indicates a continuous increase in TOC over the last decade. Fixing tropical ANT emissions reduces this trend to +0.146 $DU\ yr^{-1}$, resulting in a REF-ANT_Fix difference of +0.018 $DU\ yr^{-1}$, while fixing tropical emissions from BB increases the trend to +0.182 $DU\ yr^{-1}$, corresponding to a REF-BB_Fix difference of -0.017 $DU\ yr^{-1}$. This mismatch shows that ANT emissions have a major positive effect on the global TOC trend, while BB partly offsets this increase, possibly through enhanced chemistry with VOC and regional redistribution of O_3 production.

As expected, the influence of ANT emissions is particularly strong in the tropical and subtropical zones. The SHSAm and EQAs regions show substantial reductions in TOC trends when tropical ANT emissions are fixed, with REF-ANT_Fix differences ranging from +0.040 to +0.050 $DU\ yr^{-1}$. These regions are characterised by BB intense and biogenic emissions, rising VOCs emissions, which corresponds to NOx-limited regimes, as suggested by higher VOC/NOx ratios (Figs. 7 and 8d). Similarly, in the regions (SEAs and SAs) with rapid economic development, increasing NOx emissions, consistent with VOC-limited or transition regime (Figs. 7 and 8b). In these regimes, increases in NOx from ANT effectively enhance O_3 production, explaining the high sensitivity of TOC trends to ANT emissions.

On the other hand, fixing emissions from BB leads to a systematic decrease in TOC trends in most tropical regions (REF-BB_Fix between -0.010 and -0.044 $DU\ yr^{-1}$), with the largest response in SAf and SHSAm. The EURO, China and TENAm regions show lower sensitivity to tropical emission disturbances (REF-ANT_Fix < 0.02 $DU\ yr^{-1}$), reflecting the greater role of regional emission controls and transport processes. Nevertheless, these regions show sustained positive trends in TOC in the REF simulation (+0.214 $DU\ yr^{-1}$ in Europe and +0.212 $DU\ yr^{-1}$ in China), consistent with the gradual transition to VOC-

https://doi.org/10.5194/egusphere-2026-1652
Preprint. Discussion started: 13 May 2026

limited regime.

A combined analysis of Table 3 with the VOC/NOx ratio time series (Fig. 8) provides a consistent chemical regime interpretation of these results. The regions showing consistently high VOC/NOx ratios (NOx-limited regime) are severely limited in NOx and therefore very sensitive to ANT NOx perturbations, which explains the large differences between REF and ANT_Fix. In contrast, regions with lower or declining VOC/NOx ratios (VOC-limited or transition regime) are less sensitive, as O_3 production is less affected by additional NOx emissions. These results suggest that the increase of the TOC tropical region is due mainly by the ANT emission compared to BB emissions. Note that the ANT tropical emissions increase has a marginal impact on the increase of TOC on the global scale according to Table 3. Meanwhile, BB emissions play a minor but nonetheless important role in modulating regional O_3 production and partially offsetting ANT increases. This combined perspective highlights the crucial importance of controlling ANT NOx emissions in tropical regions in order to constrain future growth in tropospheric O_3, especially in regions where high VOCs availability maintains high O_3 production efficiency.

5 Conclusions

Tropospheric O_3 is a secondary pollutant produced by the photochemical oxidation of VOCs in the presence of NOx. Zhang et al. (2016) highlighted that, over the last decade, emissions of O_3 precursors have shifted from the mid-latitudes toward equatorial regions, causing to an increase in global tropospheric O_3 burden, as tropical regions provide circumstances that favour O_3 photochemistry.

We present in this study the findings of a modelling study to assess the impact of the evolution for two surface emissions in the tropics upon tropospheric and chemical regimes of O_3 through numerical simulations of the last decade with the CTM GEOS-Chem using the best emissions inventories for biomass-burning (BB) and anthropogenic (ANT) sources.

We have performed four 15-years full-chemistry simulations with the GC model at $2° \times 2.5°$ of horizontal resolution using the MERRA-2 as meteorological forcing in order to evaluate and constrain emission inventories. The GFAS and FINN v2.5 for BB emissions inventories and the CAMS-ANT v6.2 and CEDS v2 for ANT emissions were evaluated against OMI for NO_2 and HCHO and against SOFRID-IASI retrievals for TOC and CO columns. From this model-evaluation we concluded that the combination of GFAS for BB and CAMS for ANT emission provides the best overall agreement with the selected satellite observations. GFAS clearly improves the representation of the variabilities of HCHO and CO columns compared to FINN which largely overestimates these variabilities. The use of CAMS allows reducing the positive biases of NO_2 columns over highly polluted Asian regions compared to CEDS.

The REF simulation (GFAS & CAMS couple of emission) reproduces the annual spatial distributions of NO_2 and HCHO reasonably well compared to OMI retrievals. TOC and CO columns are also consistent with SOFRID. Significant TOC overestimations are found around the tropical belt, probably related to long-distance transport, particularly of burning plumes in the SH.

TOC trends [% decade^{-1}] show clear regional heterogeneity. Strong positive trends occur over SEAs and EQAs regions. These increases are consistent with rapid regional increase in ANT emissions and burning activity, providing a highly favourable

https://doi.org/10.5194/egusphere-2026-1652
Preprint. Discussion started: 13 May 2026

chemical environment for O_3 formation. Moderate increases of TOC are observed across the NH in mid-latitudes, reflecting hemispheric-scale transport despite emission controls. In contrast, negative trends appear in the central and eastern tropical Pacific, likely linked to ENSO variability, while the SH in mid-latitudes remain relatively stable due to lower emissions and stronger oceanic influence. Finally, a significant positive trend occurred at high latitudes in NH which may result from the transport of O_3-rich air masses from mid-latitudes towards the polar regions, as well as increased exchange between the stratosphere and troposphere. These findings are consistent with the study of Hubert et al. (in review) in their TOC trend results over the 2005-2022 period which is based on a robust product combining 10 satellite retrievals from UV-Vis and IR sensors.

Previous studies have reviewed the long-term variability of O_3 and its controlling factors (e.g., Zhang et al., 2016), highlighting the role of ANT, BB emissions, and circulation patterns. However, many of these studies relied on global-scale perturbation experiments or overall regional assessments. This current study provides an advance to our understanding by fixing emissions in tropical regions, quantifying directly the influence of tropical emission on TOC evolution, providing a more specific attribution than global-scale sensitivity tests, and clearly separating opposing O_3 trends. Throughout the results, we show that the increase in tropical TOC is driven by tropical ANT emissions, operating within predominantly VOC-limited regimes. The VOC/NOx ratio analysis reveals persistent large-scale patterns that are remarkably stable across seasons, indicating that the underlying O_3 chemistry is governed more by long-term emission characteristics than by short-term seasonal variability. Tropical regions consistently exhibit high VOC/NOx ratios, reflecting sustained biogenic and BB emissions that maintain high O_3 production efficiency in response to NOx perturbations.

On the global scale, the REF simulation shows a positive trend in TOC, which decreases when tropical ANT emissions are fixed, confirming their major role in driving long-term TOC increase. On the other hand, fixing BB emissions leads to an increase in TOC trends, suggesting that BB does not act as a main factor driving the long-term increase in tropical TOC, instead modulating O_3 production. At the regional scale, the sensitivity of O_3 trends to ANT emissions is strongest in tropical and subtropical regions such as SEAs and SAs, where high VOC availability and VOC-limited regime amplify the impact of increasing ANT NOx emissions. A next step will be necessary to take into account other sources beyond BB and ANT emissions, including biogenic emissions, emissions from soil, lightning, ships and aircraft, with the aim of determining whether anthropogenic (ANT) emissions have a major impact on TOC. An ongoing study is focusing on harmonisation of O_3 satellite products (Hubert et al., in review) which will provide a more robust basis for assessing of O_3 trends through modelling studies covering large regions and at the global scale.

The analysis reported in this study is focused on total VOCs and NOx from the model. This approach differs with previous studies (Elshorbany et al., 2024; Tian et al., 2025), which relied on satellite-derived HCHO and NO_2 as proxy indicators to diagnose the O_3 chemical regime, given the observational limitations of certain VOCs species. Overall, the analysis of the VOC/NOx ratio compared to the HCHO/NO_2 ratio is generally consistent, leading to the conclude that the HCHO/NO_2 ratio may be used as an indicator to characterise the chemical regime of O_3 production if we consider only the reactive VOCs used in this study, whereas it would be a constraint if we included all VOCs from the GC-model in the VOC/NOx ratio calculation. It would also be useful to take into account the progress made in emissions inventories and GEOS-Chem model updates, as incorporating these improvements may further enhance the accuracy and reliability of the results.

https://doi.org/10.5194/egusphere-2026-1652
Preprint. Discussion started: 13 May 2026

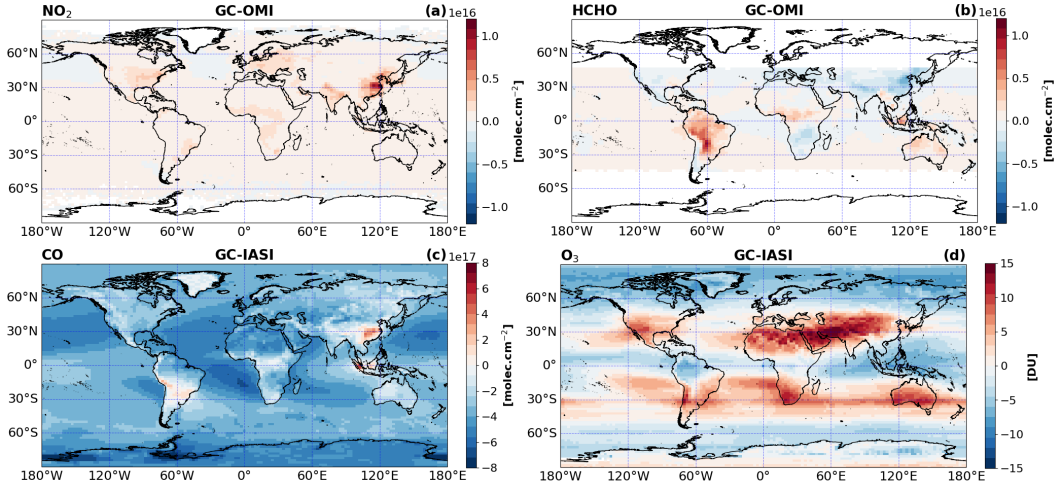

Figure A1. Difference in the tropospheric column between GC and OMI for NO_2 (a), HCHO (b) in $\mathrm{molec.cm^{-2}}$, Difference in the Total columns of CO ($\mathrm{molec.cm^{-2}}$) (c) and TOC (DU) (d) between GC and IASI over the 2008-2019 period.

Data availability. Level 3 (L3) dataset from OMI used in this paper can be accessed at https://doi.org/10.21944/cci-no2-omi-l3 (OMI NO_2) and at https://doi.org/10.18758/BF145884 (OMI HCHO). The generated L3 dataset will be made available on the ESA Climate Change Initiative Open Data portal. The SOFRID dataset are available for the whole period from the Service de données de l'Observatoire Midi-Pyrénées (https://iasi-sofrid.sedoo.fr/, last access: 24 March 2026).

Appendix A

https://doi.org/10.5194/egusphere-2026-1652
Preprint. Discussion started: 13 May 2026

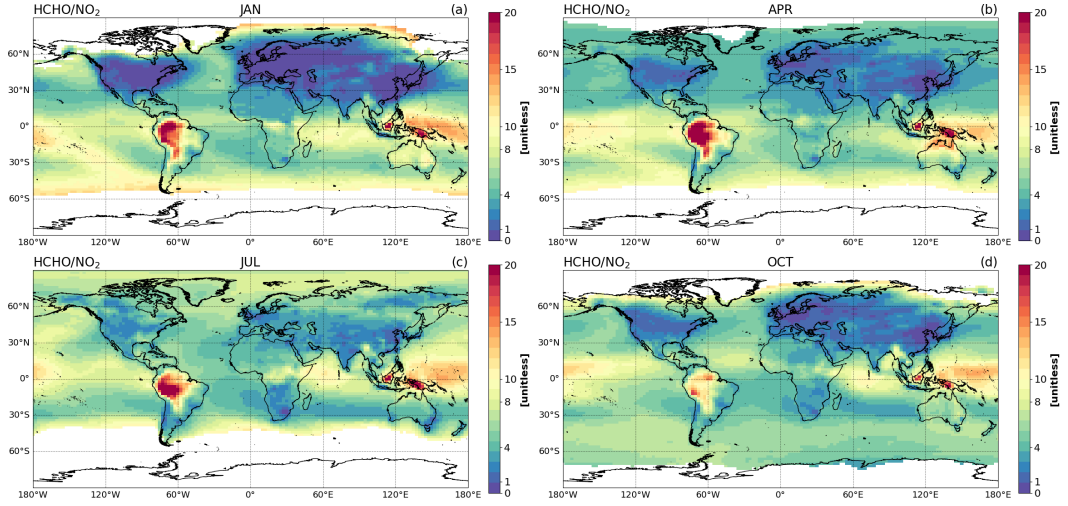

Figure A2. Monthly averages of $HCHO/NO_2$ in the tropospheric column derived from REF simulation for the period 2007-2021. Panel (a) shows the climatological mean ratio for all January months, (b) for April, (c) for July, and (d) for October. ratio. The ratio is computed by taking account the NO_2 tropospheric column above 1E+14 $\mathrm{molec.cm^{-2}}$. The "white" colour range is mainly due to the lower NO_2 tropospheric column. The production of NOx species by photochemical reactions is slightly reduced.

Author contributions. HN, BS and BB designed the research and the numerical experiments. The GEOS-Chem model installation and the simulations were carried out by HN, with help from BS and BB. The OMI tropospheric column of NO_2 and HCHO were processed and provided by IA and IDS. The total columns of CO and TOC retrieved by SOFRID were provided by ELF. The paper was written by HN, all authors collaborated in the reviewing and editing of the article.

Competing interests. At least one of the (co-)authors is a member of the editorial board of Atmospheric Chemistry and Physics.

Acknowledgements. This research was carried out in the framework of the ESA CCI+ Precursors for Aerosol and Ozone project which financed Herizo Narivelo. The authors acknowledge funding from the ESA CCI+ Precursors for Aerosol and Ozone project and the Université de Toulouse for the administration of Herizo Narivelo's contract.
The IASI mission is a joint mission of EUMETSAT and the Centre National d'Etudes Spatiales (CNES, France). The L1C operational IASI data were distributed in near real time by EUMETSAT through the EUMETCast system distribution.
This work was granted access to the HPC resources of CALMIP supercomputing center under the allocation 2024-[P24038].

https://doi.org/10.5194/egusphere-2026-1652
Preprint. Discussion started: 13 May 2026

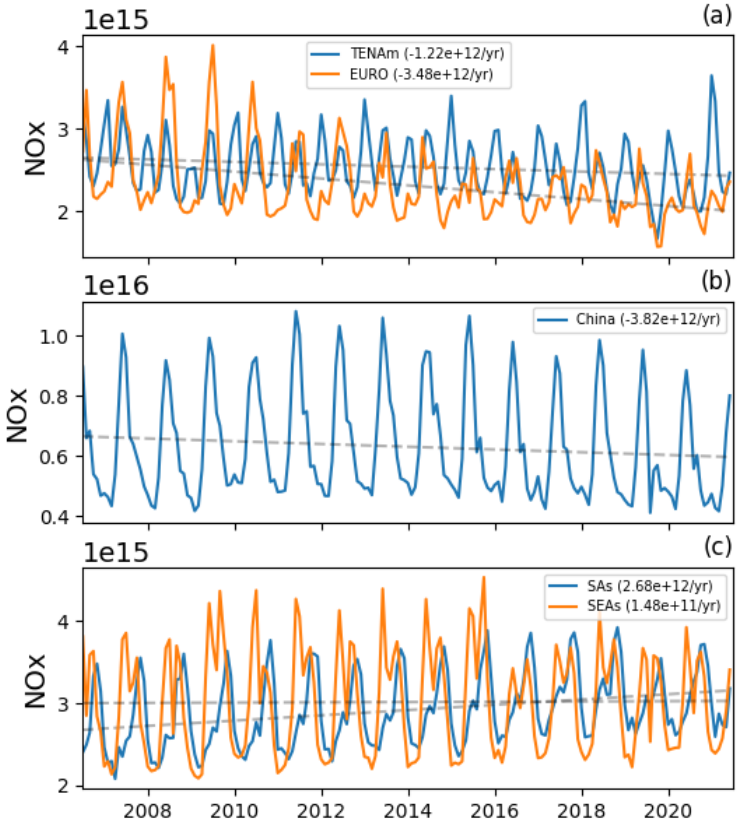

Figure A3. Time series of the NOx between 2007 and 2021, as derived from GC for the TENAm and EURO regions (a), China region (b) and for SAs and SEAs regions (c). All colored dashed lines correspond to their respective linear trends.

https://doi.org/10.5194/egusphere-2026-1652
Preprint. Discussion started: 13 May 2026

References

Ainsworth, E. A., Yendrek, C. R., Sitch, S., Collins, W. J., and Emberson, L. D.: The Effects of Tropospheric Ozone on Net Primary Productivity and Implications for Climate Change*, Annual Review of Plant Biology, 63, 637–661, https://doi.org/https://doi.org/10.1146/annurev-arplant-042110-103829, 2012.

Anglou, I., Glissenaar, I. A., Boersma, K. F., and Eskes, H.: ESA CCI+ OMI L3 monthly mean NO_2 columns [Data set], https://doi.org/10.21944/cci-no2-omi-l3, 2024.

Barret, B., Emili, E., and Le Flochmoen, E.: A tropopause-related climatological a priori profile for IASI-SOFRID ozone retrievals: improvements and validation, Atmospheric Measurement Techniques, 13, 5237–5257, https://doi.org/10.5194/amt-13-5237-2020, 2020.

Barret, B., Loicq, P., Le Flochmoën, E., Bennouna, Y., Hadji-Lazaro, J., Hurtmans, D., and Sauvage, B.: Validation of 12 years (2008–2019) of IASI-A CO with IAGOS aircraft observations, Atmospheric Measurement Techniques, 18, 129–149, https://doi.org/10.5194/amt-18-129-2025, 2025.

Bates, D. V.: Ambient Ozone and Mortality, Epidemiology, 16, 427–429, https://doi.org/10.1097/01.ede.0000165793.71278.ec, 2005.

Bey, I., Jacob, D. J., Yantosca, R. M., Logan, J. A., Field, B. D., Fiore, A. M., Li, Q., Liu, H. Y., Mickley, L. J., and Schultz, M. G.: Global modeling of tropospheric chemistry with assimilated meteorology: Model description and evaluation, Journal of Geophysical Research: Atmospheres, 106, 23 073–23 095, https://doi.org/10.1029/2001JD000807, 2001.

Boersma, K. F., Vinken, G. C. M., and Eskes, H. J.: Representativeness errors in comparing chemistry transport and chemistry climate models with satellite UV–Vis tropospheric column retrievals, Geoscientific Model Development, 9, 875–898, https://doi.org/10.5194/gmd-9-875-2016, 2016.

Bourgeois, I., Peischl, J., Neuman, J. A., Brown, S. S., Thompson, C. R., Aikin, K. C., Allen, H. M., Angot, H., Apel, E. C., Baublitz, C. B., Brewer, J. F., Campuzano-Jost, P., Commane, R., Crounse, J. D., Daube, B. C., DiGangi, J. P., Diskin, G. S., Emmons, L. K., Fiore, A. M., Gkatzelis, G. I., Hills, A., Hornbrook, R. S., Huey, L. G., Jimenez, J. L., Kim, M., Lacey, F., McKain, K., Murray, L. T., Nault, B. A., Parrish, D. D., Ray, E., Sweeney, C., Tanner, D., Wofsy, S. C., and Ryerson, T. B.: Large contribution of biomass burning emissions to ozone throughout the global remote troposphere, Proceedings of the National Academy of Sciences, 118, e2109628 118, https://doi.org/10.1073/pnas.2109628118, 2021.

Bowman, H., Turnock, S., Bauer, S. E., Tsigaridis, K., Deushi, M., Oshima, N., O'Connor, F. M., Horowitz, L., Wu, T., Zhang, J., Kubistin, D., and Parrish, D. D.: Changes in anthropogenic precursor emissions drive shifts in the ozone seasonal cycle throughout the northern midlatitude troposphere, Atmospheric Chemistry and Physics, 22, 3507–3524, https://doi.org/10.5194/acp-22-3507-2022, 2022.

Brunekreef, B. and Holgate, S. T.: Air pollution and health, The lancet, 360, 1233–1242, 2002.

Chen, Y., Turnock, S. T., Scott, C. E., and Arnold, S. R.: Radiative Response to Large Decline in Anthropogenic Emissions From China Between 2008 and 2016 Is Modified by Simultaneous Biomass Burning Emission Changes, Journal of Geophysical Research: Atmospheres, 130, e2025JD044 548, https://doi.org/10.1029/2025JD044548, e2025JD044548 2025JD044548, 2025.

Christiansen, A., Mickley, L. J., Liu, J., Oman, L. D., and Hu, L.: Multidecadal increases in global tropospheric ozone derived from ozonesonde and surface site observations: can models reproduce ozone trends?, Atmospheric Chemistry and Physics, 22, 14 751–14 782, https://doi.org/10.5194/acp-22-14751-2022, 2022.

Clerbaux, C., Boynard, A., Clarisse, L., George, M., Hadji-Lazaro, J., Herbin, H., Hurtmans, D., Pommier, M., Razavi, A., Turquety, S., Wespes, C., and Coheur, P.-F.: Monitoring of atmospheric composition using the thermal infrared IASI/MetOp sounder, Atmospheric Chemistry and Physics, 9, 6041–6054, https://doi.org/10.5194/acp-9-6041-2009, 2009.

https://doi.org/10.5194/egusphere-2026-1652
Preprint. Discussion started: 13 May 2026

Crippa, M., Janssens-Maenhout, G., Dentener, F., Guizzardi, D., Sindelarova, K., Muntean, M., Van Dingenen, R., and Granier, C.: Forty years of improvements in European air quality: regional policy-industry interactions with global impacts, Atmospheric Chemistry and Physics, 16, 3825–3841, https://doi.org/10.5194/acp-16-3825-2016, 2016.

De Smedt, I., Theys, N., Yu, H., Danckaert, T., Lerot, C., Compernolle, S., Van Roozendael, M., Richter, A., Hilboll, A., Peters, E., Pedergnana, M., Loyola, D., Beirle, S., Wagner, T., Eskes, H., van Geffen, J., Boersma, K. F., and Veefkind, P.: Algorithm theoretical baseline for formaldehyde retrievals from S5P TROPOMI and from the QA4ECV project, Atmospheric Measurement Techniques, 11, 2395–2426, https://doi.org/10.5194/amt-11-2395-2018, 2018.

De Smedt, I., Pinardi, G., Vigouroux, C., Compernolle, S., Bais, A., Benavent, N., Boersma, F., Chan, K.-L., Donner, S., Eichmann, K.-U., Hedelt, P., Hendrick, F., Irie, H., Kumar, V., Lambert, J.-C., Langerock, B., Lerot, C., Liu, C., Loyola, D., Piters, A., Richter, A., Rivera Cárdenas, C., Romahn, F., Ryan, R. G., Sinha, V., Theys, N., Vlietinck, J., Wagner, T., Wang, T., Yu, H., and Van Roozendael, M.: Comparative assessment of TROPOMI and OMI formaldehyde observations and validation against MAX-DOAS network column measurements, Atmospheric Chemistry and Physics, 21, 12 561–12 593, https://doi.org/10.5194/acp-21-12561-2021, 2021.

De Smedt, I., Vlietinck, J., YU, H., Theys, N., Danckaert, T., and Van Roozendael, M.: CCI+P HCHO tropospheric column L3 data from OMI, v2, https://doi.org/10.18758/BF145884, 2025.

De Wachter, E., Barret, B., Le Flochmoën, E., Pavelin, E., Matricardi, M., Clerbaux, C., Hadji-Lazaro, J., George, M., Hurtmans, D., Coheur, P.-F., Nedelec, P., and Cammas, J. P.: Retrieval of MetOp-A/IASI CO profiles and validation with MOZAIC data, Atmospheric Measurement Techniques, 5, 2843–2857, https://doi.org/10.5194/amt-5-2843-2012, 2012.

Dufour, G., Eremenko, M., Griesfeller, A., Barret, B., LeFlochmoën, E., Clerbaux, C., Hadji-Lazaro, J., Coheur, P.-F., and Hurtmans, D.: Validation of three different scientific ozone products retrieved from IASI spectra using ozonesondes, Atmospheric Measurement Techniques, 5, 611–630, https://doi.org/10.5194/amt-5-611-2012, 2012.

Duncan, B. N., Yoshida, Y., Olson, J. R., Sillman, S., Martin, R. V., Lamsal, L., Hu, Y., Pickering, K. E., Retscher, C., Allen, D. J., and Crawford, J. H.: Application of OMI observations to a space-based indicator of NOx and VOC controls on surface ozone formation, Atmospheric Environment, 44, 2213–2223, https://doi.org/https://doi.org/10.1016/j.atmosenv.2010.03.010, 2010.

Eastham, S. D., Weisenstein, D. K., and Barrett, S. R.: Development and evaluation of the unified tropospheric–stratospheric chemistry extension (UCX) for the global chemistry-transport model GEOS-Chem, Atmospheric Environment, 89, 52–63, https://doi.org/https://doi.org/10.1016/j.atmosenv.2014.02.001, 2014.

Eastham, S. D., Long, M. S., Keller, C. A., Lundgren, E., Yantosca, R. M., Zhuang, J., Li, C., Lee, C. J., Yannetti, M., Auer, B. M., Clune, T. L., Kouatchou, J., Putman, W. M., Thompson, M. A., Trayanov, A. L., Molod, A. M., Martin, R. V., and Jacob, D. J.: GEOS-Chem High Performance (GCHP v11-02c): a next-generation implementation of the GEOS-Chem chemical transport model for massively parallel applications, Geoscientific Model Development, 11, 2941–2953, https://doi.org/10.5194/gmd-11-2941-2018, 2018.

Elshorbany, Y., Ziemke, J. R., Strode, S., Petetin, H., Miyazaki, K., De Smedt, I., Pickering, K., Seguel, R. J., Worden, H., Emmerichs, T., Taraborrelli, D., Cazorla, M., Fadnavis, S., Buchholz, R. R., Gaubert, B., Rojas, N. Y., Nogueira, T., Salameh, T., and Huang, M.: Tropospheric ozone precursors: global and regional distributions, trends, and variability, Atmospheric Chemistry and Physics, 24, 12 225–12 257, https://doi.org/10.5194/acp-24-12225-2024, 2024.

EU: Proposal for a directive of the European Parliament and of the Council on the reduction of national emissions of certain atmospheric pollutants and amending Directive 2003/35/EC, Official Journal of the European Union, 2003.

Fisher, J. A., Jacob, D. J., Wang, Q., Bahreini, R., Carouge, C. C., Cubison, M. J., Dibb, J. E., Diehl, T., Jimenez, J. L., Leibensperger, E. M., Lu, Z., Meinders, M. B., Pye, H. O., Quinn, P. K., Sharma, S., Streets, D. G., van Donkelaar, A., and Yantosca, R. M.:

https://doi.org/10.5194/egusphere-2026-1652
Preprint. Discussion started: 13 May 2026

Sources, distribution, and acidity of sulfate–ammonium aerosol in the Arctic in winter–spring, Atmospheric Environment, 45, 7301–7318, https://doi.org/https://doi.org/10.1016/j.atmosenv.2011.08.030, 2011.

Froidevaux, L., Kinnison, D. E., Gaubert, B., Schwartz, M. J., Livesey, N. J., Read, W. G., Bardeen, C. G., Ziemke, J. R., and Fuller, R. A.: Tropical upper-tropospheric trends in ozone and carbon monoxide (2005–2020): observational and model results, Atmospheric Chemistry and Physics, 25, 597–624, https://doi.org/10.5194/acp-25-597-2025, 2025.

Gaudel, A., Cooper, O. R., Ancellet, G., Barret, B., Boynard, A., Burrows, J. P., Clerbaux, C., Coheur, P.-F., Cuesta, J., Cuevas, E., Doniki, S., Dufour, G., Ebojie, F., Foret, G., Garcia, O., Granados-Muñoz, M. J., Hannigan, J. W., Hase, F., Hassler, B., Huang, G., Hurtmans, D., Jaffe, D., Jones, N., Kalabokas, P., Kerridge, B., Kulawik, S., Latter, B., Leblanc, T., Le Flochmoën, E., Lin, W., Liu, J., Liu, X., Mahieu, E., McClure-Begley, A., Neu, J. L., Osman, M., Palm, M., Petetin, H., Petropavlovskikh, I., Querel, R., Rahpoe, N., Rozanov, A., Schultz, M. G., Schwab, J., Siddans, R., Smale, D., Steinbacher, M., Tanimoto, H., Tarasick, D. W., Thouret, V., Thompson, A. M., Trickl, T., Weatherhead, E., Wespes, C., Worden, H. M., Vigouroux, C., Xu, X., Zeng, G., and Ziemke, J.: Tropospheric Ozone Assessment Report: Present-day distribution and trends of tropospheric ozone relevant to climate and global atmospheric chemistry model evaluation, Elementa: Science of the Anthropocene, 6, 39, https://doi.org/10.1525/elementa.291, 2018.

Gaudel, A., Bourgeois, I., Li, M., Chang, K.-L., Ziemke, J., Sauvage, B., Stauffer, R. M., Thompson, A. M., Kollonige, D. E., Smith, N., Hubert, D., Keppens, A., Cuesta, J., Heue, K.-P., Veefkind, P., Aikin, K., Peischl, J., Thompson, C. R., Ryerson, T. B., Frost, G. J., McDonald, B. C., and Cooper, O. R.: Tropical tropospheric ozone distribution and trends from in situ and satellite data, Atmospheric Chemistry and Physics, 24, 9975–10 000, https://doi.org/10.5194/acp-24-9975-2024, 2024.

Geddes, J. A., Murphy, J. G., O'Brien, J. M., and Celarier, E. A.: Biases in long-term NO2 averages inferred from satellite observations due to cloud selection criteria, Remote Sensing of Environment, 124, 210–216, https://doi.org/https://doi.org/10.1016/j.rse.2012.05.008, 2012.

Gelaro, R., McCarty, W., Suárez, M. J., Todling, R., Molod, A., Takacs, L., Randles, C. A., Darmenov, A., Bosilovich, M. G., Reichle, R., Wargan, K., Coy, L., Cullather, R., Draper, C., Akella, S., Buchard, V., Conaty, A., da Silva, A. M., Gu, W., Kim, G.-K., Koster, R., Lucchesi, R., Merkova, D., Nielsen, J. E., Partyka, G., Pawson, S., Putman, W., Rienecker, M., Schubert, S. D., Sienkiewicz, M., and Zhao, B.: The Modern-Era Retrospective Analysis for Research and Applications, Version 2 (MERRA-2), Journal of Climate, 30, 5419 – 5454, https://doi.org/10.1175/JCLI-D-16-0758.1, 2017.

Goldberg, D. L., Lamsal, L. N., Loughner, C. P., Swartz, W. H., Lu, Z., and Streets, D. G.: A high-resolution and observationally constrained OMI NO_2 satellite retrieval, Atmospheric Chemistry and Physics, 17, 11 403–11 421, https://doi.org/10.5194/acp-17-11403-2017, 2017.

Gonzi, S., Palmer, P. I., Barkley, M. P., De Smedt, I., and Van Roozendael, M.: Biomass burning emission estimates inferred from satellite column measurements of HCHO: Sensitivity to co-emitted aerosol and injection height, Geophysical Research Letters, 38, https://doi.org/https://doi.org/10.1029/2011GL047890, 2011.

Granier, C., Bessagnet, B., Bond, T., D'Angiola, A., Denier van der Gon, H., Frost, G., Heil, A., Kaiser, J., Kinne, S., Klimont, Z., Kloster, S., Lamarque, J.-F., Liousse, C., Masui, T., Meleux, F., Mieville, A., Ohara, T., Raut, J.-C., Riahi, K., and Vuuren, D.: Evolution of anthropogenic and biomass burning emissions of air pollutants at global and regional scales during the 1980–2010 period, Climatic Change, 109, 163–190, https://doi.org/10.1007/s10584-011-0154-1, 2011.

Guenther, A., Karl, T., Harley, P., Wiedinmyer, C., Palmer, P. I., and Geron, C.: Estimates of global terrestrial isoprene emissions using MEGAN (Model of Emissions of Gases and Aerosols from Nature), Atmospheric Chemistry and Physics, 6, 3181–3210, https://doi.org/10.5194/acp-6-3181-2006, 2006.

https://doi.org/10.5194/egusphere-2026-1652
Preprint. Discussion started: 13 May 2026

Guenther, A. B., Jiang, X., Heald, C. L., Sakulyanontvittaya, T., Duhl, T., Emmons, L. K., and Wang, X.: The Model of Emissions of Gases and Aerosols from Nature version 2.1 (MEGAN2.1): an extended and updated framework for modeling biogenic emissions, Geoscientific Model Development, 5, 1471–1492, https://doi.org/10.5194/gmd-5-1471-2012, 2012.

Hammer, M. S., van Donkelaar, A., Li, C., Lyapustin, A., Sayer, A. M., Hsu, N. C., Levy, R. C., Garay, M. J., Kalashnikova, O. V., Kahn, R. A., Brauer, M., Apte, J. S., Henze, D. K., Zhang, L., Zhang, Q., Ford, B., Pierce, J. R., and Martin, R. V.: Global Estimates and Long-Term Trends of Fine Particulate Matter Concentrations (1998–2018), Environmental Science & Technology, 54, 7879–7890, https://doi.org/10.1021/acs.est.0c01764, pMID: 32491847, 2020.

Herman, J., Abuhassan, N., Kim, J., Kim, J., Dubey, M., Raponi, M., and Tzortziou, M.: Underestimation of column NO_2 amounts from the OMI satellite compared to diurnally varying ground-based retrievals from multiple PANDORA spectrometer instruments, Atmospheric Measurement Techniques, 12, 5593–5612, https://doi.org/10.5194/amt-12-5593-2019, 2019.

Hoesly, R. M., Smith, S. J., Feng, L., Klimont, Z., Janssens-Maenhout, G., Pitkanen, T., Seibert, J. J., Vu, L., Andres, R. J., Bolt, R. M., Bond, T. C., Dawidowski, L., Kholod, N., Kurokawa, J.-I., Li, M., Liu, L., Lu, Z., Moura, M. C. P., O'Rourke, P. R., and Zhang, Q.: Historical (1750–2014) anthropogenic emissions of reactive gases and aerosols from the Community Emissions Data System (CEDS), Geoscientific Model Development, 11, 369–408, https://doi.org/10.5194/gmd-11-369-2018, 2018.

Hubert, D., Miyazaki, K., Dufour, G., Pennington, E., Sofieva, V., and more authors: Tropospheric Ozone Assessment Report II: Past and present tropospheric ozone using satellite observations, under review in the Royal Society Publishing, in review.

Hudman, R. C., Moore, N. E., Mebust, A. K., Martin, R. V., Russell, A. R., Valin, L. C., and Cohen, R. C.: Steps towards a mechanistic model of global soil nitric oxide emissions: implementation and space based-constraints, Atmospheric Chemistry and Physics, 12, 7779–7795, https://doi.org/10.5194/acp-12-7779-2012, 2012.

Huijnen, V., Pozzer, A., Arteta, J., Brasseur, G., Bouarar, I., Chabrillat, S., Christophe, Y., Doumbia, T., Flemming, J., Guth, J., Josse, B., Karydis, V. A., Marécal, V., and Pelletier, S.: Quantifying uncertainties due to chemistry modelling – evaluation of tropospheric composition simulations in the CAMS model (cycle 43R1), Geoscientific Model Development, 12, 1725–1752, https://doi.org/10.5194/gmd-12-1725-2019, 2019.

IPCC: The Physical Science Basis. Contribution of Working Group I to the Fourth Assessment Report of the Intergovernmental Panel on Climate Change. Chapter 1, Historical Overview of Climate change, in: Intergovernmental Panel on Climate Change Climate change: The Physical Science Basis, Contribution of Working Group I to the Fourth Assessment Report of the IPCC, Cambridge University Press, Cambridge, 2007.

IPCC: Climate Change 2021. The Physical Science Basis: Working Group I Contribution to the Sixth Assessment Report of the Intergovernmental Panel on Climate Change, Cambridge University Press, Cambridge, 2023.

Jacob, D. and Winner, D.: Effect of Climate Change on Air Quality, Atmos. Environ., 43, https://doi.org/10.1016/j.atmosenv.2008.09.051, 2009.

Jaffe, D. A., Cooper, O. R., Fiore, A. M., Henderson, B. H., Tonnesen, G. S., Russell, A. G., Henze, D. K., Langford, A. O., Lin, M., and Moore, T.: Scientific assessment of background ozone over the U.S.: Implications for air quality management, Elementa: Science of the Anthropocene, 6, 56, https://doi.org/10.1525/elementa.309, 2018.

Jiang, Z., Zhu, R., Miyazaki, K., McDonald, B. C., Klimont, Z., Zheng, B., Boersma, K. F., Zhang, Q., Worden, H., Worden, J. R., Henze, D. K., Jones, D. B. A., Denier van der Gon, H. A. C., and Eskes, H.: Decadal Variabilities in Tropospheric Nitrogen Oxides Over United States, Europe, and China, Journal of Geophysical Research: Atmospheres, 127, e2021JD035 872, https://doi.org/https://doi.org/10.1029/2021JD035872, e2021JD035872 2021JD035872, 2022.

https://doi.org/10.5194/egusphere-2026-1652
Preprint. Discussion started: 13 May 2026

Kaiser, J. W., Heil, A., Andreae, M. O., Benedetti, A., Chubarova, N., Jones, L., Morcrette, J.-J., Razinger, M., Schultz, M. G., Suttie, M., and van der Werf, G. R.: Biomass burning emissions estimated with a global fire assimilation system based on observed fire radiative power, Biogeosciences, 9, 527–554, https://doi.org/10.5194/bg-9-527-2012, 2012.

Keller, C. A., Long, M. S., Yantosca, R. M., Da Silva, A. M., Pawson, S., and Jacob, D. J.: HEMCO v1.0: a versatile, ESMF-compliant component for calculating emissions in atmospheric models, Geoscientific Model Development, 7, 1409–1417, https://doi.org/10.5194/gmd-7-1409-2014, 2014.

Kim, H., Park, R. J., Kim, S., Brune, W. H., Diskin, G. S., Fried, A., Hall, S. R., Weinheimer, A. J., Wennberg, P., Wisthaler, A., Blake, D. R., and Ullmann, K.: Observed versus simulated OH reactivity during KORUS-AQ campaign: Implications for emission inventory and chemical environment in East Asia, Elementa: Science of the Anthropocene, 10, 00 030, https://doi.org/10.1525/elementa.2022.00030, 2022.

Kleipool, Q., Rozemeijer, N., van Hoek, M., Leloux, J., Loots, E., Ludewig, A., van der Plas, E., Adrichem, D., Harel, R., Spronk, S., ter Linden, M., Jaross, G., Haffner, D., Veefkind, P., and Levelt, P. F.: Ozone Monitoring Instrument (OMI) collection 4: establishing a 17-year-long series of detrended level-1b data, Atmospheric Measurement Techniques, 15, 3527–3553, https://doi.org/10.5194/amt-15-3527-2022, 2022.

Kopacz, M., Jacob, D. J., Fisher, J. A., Logan, J. A., Zhang, L., Megretskaia, I. A., Yantosca, R. M., Singh, K., Henze, D. K., Burrows, J. P., Buchwitz, M., Khlystova, I., McMillan, W. W., Gille, J. C., Edwards, D. P., Eldering, A., Thouret, V., and Nedelec, P.: Global estimates of CO sources with high resolution by adjoint inversion of multiple satellite datasets (MOPITT, AIRS, SCIAMACHY, TES), Atmospheric Chemistry and Physics, 10, 855–876, https://doi.org/10.5194/acp-10-855-2010, 2010.

Lathière, J., Hauglustaine, D. A., Friend, A. D., De Noblet-Ducoudré, N., Viovy, N., and Folberth, G. A.: Impact of climate variability and land use changes on global biogenic volatile organic compound emissions, Atmospheric Chemistry and Physics, 6, 2129–2146, https://doi.org/10.5194/acp-6-2129-2006, 2006.

Levelt, P., van den Oord, G., Dobber, M., Malkki, A., Visser, H., de Vries, J., Stammes, P., Lundell, J., and Saari, H.: The ozone monitoring instrument, IEEE Transactions on Geoscience and Remote Sensing, 44, 1093–1101, https://doi.org/10.1109/TGRS.2006.872333, 2006.

Levelt, P. F., Joiner, J., Tamminen, J., Veefkind, J. P., Bhartia, P. K., Stein Zweers, D. C., Duncan, B. N., Streets, D. G., Eskes, H., van der A, R., McLinden, C., Fioletov, V., Carn, S., de Laat, J., DeLand, M., Marchenko, S., McPeters, R., Ziemke, J., Fu, D., Liu, X., Pickering, K., Apituley, A., González Abad, G., Arola, A., Boersma, F., Chan Miller, C., Chance, K., de Graaf, M., Hakkarainen, J., Hassinen, S., Ialongo, I., Kleipool, Q., Krotkov, N., Li, C., Lamsal, L., Newman, P., Nowlan, C., Suleiman, R., Tilstra, L. G., Torres, O., Wang, H., and Wargan, K.: The Ozone Monitoring Instrument: overview of 14 years in space, Atmospheric Chemistry and Physics, 18, 5699–5745, https://doi.org/10.5194/acp-18-5699-2018, 2018.

Li, K., Jacob, D. J., Liao, H., Shen, L., Zhang, Q., and Bates, K. H.: Anthropogenic drivers of 2013–2017 trends in summer surface ozone in China, Proceedings of the National Academy of Sciences, 116, 422–427, https://doi.org/10.1073/pnas.1812168116, 2019.

Li, Y., Xia, Y., Xie, F., and Yan, Y.: Influence of stratosphere-troposphere exchange on long-term trends of surface ozone in CMIP6, Atmospheric Research, 297, 107 086, https://doi.org/https://doi.org/10.1016/j.atmosres.2023.107086, 2024.

Lin, H., Jacob, D. J., Lundgren, E. W., Sulprizio, M. P., Keller, C. A., Fritz, T. M., Eastham, S. D., Emmons, L. K., Campbell, P. C., Baker, B., Saylor, R. D., and Montuoro, R.: Harmonized Emissions Component (HEMCO) 3.0 as a versatile emissions component for atmospheric models: application in the GEOS-Chem, NASA GEOS, WRF-GC, CESM2, NOAA GEFS-Aerosol, and NOAA UFS models, Geoscientific Model Development, 14, 5487–5506, https://doi.org/10.5194/gmd-14-5487-2021, 2021.

https://doi.org/10.5194/egusphere-2026-1652
Preprint. Discussion started: 13 May 2026

Lin, H., Emmons, L. K., Lundgren, E. W., Yang, L. H., Feng, X., Dang, R., Zhai, S., Tang, Y., Kelp, M. M., Colombi, N. K., Eastham, S. D., Fritz, T. M., and Jacob, D. J.: Intercomparison of GEOS-Chem and CAM-chem tropospheric oxidant chemistry within the Community Earth System Model version 2 (CESM2), Atmospheric Chemistry and Physics, 24, 8607–8624, https://doi.org/10.5194/acp-24-8607-2024, 2024.

Liu, H., Jacob, D. J., Bey, I., and Yantosca, R. M.: Constraints from 210Pb and 7Be on wet deposition and transport in a global three-dimensional chemical tracer model driven by assimilated meteorological fields, Journal of Geophysical Research: Atmospheres, 106, 12 109–12 128, https://doi.org/https://doi.org/10.1029/2000JD900839, 2001.

Martin, R. V., Chance, K., Jacob, D. J., Kurosu, T. P., Spurr, R. J. D., Bucsela, E., Gleason, J. F., Palmer, P. I., Bey, I., Fiore, A. M., Li, Q., Yantosca, R. M., and Koelemeijer, R. B. A.: An improved retrieval of tropospheric nitrogen dioxide from GOME, Journal of Geophysical Research: Atmospheres, 107, ACH 9–1–ACH 9–21, https://doi.org/https://doi.org/10.1029/2001JD001027, 2002.

Martin, R. V., Fiore, A. M., and Van Donkelaar, A.: Space-based diagnosis of surface ozone sensitivity to anthropogenic emissions, Geophysical Research Letters, 31, https://doi.org/https://doi.org/10.1029/2004GL019416, 2004.

McDuffie, E. E., Smith, S. J., O'Rourke, P., Tibrewal, K., Venkataraman, C., Marais, E. A., Zheng, B., Crippa, M., Brauer, M., and Martin, R. V.: A global anthropogenic emission inventory of atmospheric pollutants from sector- and fuel-specific sources (1970–2017): an application of the Community Emissions Data System (CEDS), Earth System Science Data, 12, 3413–3442, https://doi.org/10.5194/essd-12-3413-2020, 2020.

Millet, D. B., Jacob, D. J., Turquety, S., Hudman, R. C., Wu, S., Fried, A., Walega, J., Heikes, B. G., Blake, D. R., Singh, H. B., Anderson, B. E., and Clarke, A. D.: Formaldehyde distribution over North America: Implications for satellite retrievals of formaldehyde columns and isoprene emission, Journal of Geophysical Research: Atmospheres, 111, https://doi.org/https://doi.org/10.1029/2005JD006853, 2006.

Monks, P. S., Archibald, A. T., Colette, A., Cooper, O., Coyle, M., Derwent, R., Fowler, D., Granier, C., Law, K. S., Mills, G. E., Stevenson, D. S., Tarasova, O., Thouret, V., von Schneidemesser, E., Sommariva, R., Wild, O., and Williams, M. L.: Tropospheric ozone and its precursors from the urban to the global scale from air quality to short-lived climate forcer, Atmospheric Chemistry and Physics, 15, 8889–8973, https://doi.org/10.5194/acp-15-8889-2015, 2015.

Murray, L. T., Jacob, D. J., Logan, J. A., Hudman, R. C., and Koshak, W. J.: Optimized regional and interannual variability of lightning in a global chemical transport model constrained by LIS/OTD satellite data, Journal of Geophysical Research: Atmospheres, 117, https://doi.org/https://doi.org/10.1029/2012JD017934, 2012.

Palmer, P. I., Jacob, D. J., Fiore, A. M., Martin, R. V., Chance, K., and Kurosu, T. P.: Mapping isoprene emissions over North America using formaldehyde column observations from space, Journal of Geophysical Research: Atmospheres, 108, https://doi.org/https://doi.org/10.1029/2002JD002153, 2003.

Park, R. J., Jacob, D. J., Field, B. D., Yantosca, R. M., and Chin, M.: Natural and transboundary pollution influences on sulfate-nitrate-ammonium aerosols in the United States: Implications for policy, Journal of Geophysical Research: Atmospheres, 109, https://doi.org/https://doi.org/10.1029/2003JD004473, 2004.

Parrish, D. D., Derwent, R. G., and Staehelin, J.: Long-term changes in northern mid-latitude tropospheric ozone concentrations: Synthesis of two recent analyses, Atmospheric Environment, 248, 118 227, https://doi.org/https://doi.org/10.1016/j.atmosenv.2021.118227, 2021.

Pope, R. J., Rap, A., Pimlott, M. A., Barret, B., Le Flochmoen, E., Kerridge, B. J., Siddans, R., Latter, B. G., Ventress, L. J., Boynard, A., Retscher, C., Feng, W., Rigby, R., Dhomse, S. S., Wespes, C., and Chipperfield, M. P.: Quantifying the tropospheric ozone radiative effect and its temporal evolution in the satellite era, Atmospheric Chemistry and Physics, 24, 3613–3626, https://doi.org/10.5194/acp-24-3613-2024, 2024.

https://doi.org/10.5194/egusphere-2026-1652
Preprint. Discussion started: 13 May 2026

Ruiz Villena, C., Anand, J. S., Leigh, R. J., Monks, P. S., Parfitt, C. E., and Vande Hey, J. D.: Discrete-wavelength DOAS NO_2 slant column retrievals from OMI and TROPOMI, Atmospheric Measurement Techniques, 13, 1735–1756, https://doi.org/10.5194/amt-13-1735-2020, 2020.

Sauvage, B., Martin, R. V., van Donkelaar, A., Liu, X., Chance, K., Jaeglé, L., Palmer, P. I., Wu, S., and Fu, T.-M.: Remote sensed and in situ constraints on processes affecting tropical tropospheric ozone, Atmospheric Chemistry and Physics, 7, 815–838, https://doi.org/10.5194/acp-7-815-2007, 2007.

Schenkeveld, V. M. E., Jaross, G., Marchenko, S., Haffner, D., Kleipool, Q. L., Rozemeijer, N. C., Veefkind, J. P., and Levelt, P. F.: In-flight performance of the Ozone Monitoring Instrument, Atmospheric Measurement Techniques, 10, 1957–1986, https://doi.org/10.5194/amt-10-1957-2017, 2017.

Seguel, R. J., Opazo, C., Cohen, Y., Cooper, O. R., Gallardo, L., Sinnhuber, B.-M., Obersteiner, F., Zahn, A., Hoor, P., Rohs, S., and Marsing, A.: Hemispheric differences in ozone across the stratosphere–troposphere exchange region, Atmospheric Chemistry and Physics, 25, 8553–8573, https://doi.org/10.5194/acp-25-8553-2025, 2025.

Shindell, D. T., Faluvegi, G., Stevenson, D. S., Krol, M. C., Emmons, L. K., Lamarque, J.-F., Pétron, G., Dentener, F. J., Ellingsen, K., Schultz, M. G., Wild, O., Amann, M., Atherton, C. S., Bergmann, D. J., Bey, I., Butler, T., Cofala, J., Collins, W. J., Derwent, R. G., Doherty, R. M., Drevet, J., Eskes, H. J., Fiore, A. M., Gauss, M., Hauglustaine, D. A., Horowitz, L. W., Isaksen, I. S. A., Lawrence, M. G., Montanaro, V., Müller, J.-F., Pitari, G., Prather, M. J., Pyle, J. A., Rast, S., Rodriguez, J. M., Sanderson, M. G., Savage, N. H., Strahan, S. E., Sudo, K., Szopa, S., Unger, N., van Noije, T. P. C., and Zeng, G.: Multimodel simulations of carbon monoxide: Comparison with observations and projected near-future changes, Journal of Geophysical Research: Atmospheres, 111, https://doi.org/10.1029/2006JD007100, 2006.

Sillman, S.: The relation between ozone, NOx and hydrocarbons in urban and polluted rural environments, Atmospheric Environment, 33, 1821–1845, https://doi.org/https://doi.org/10.1016/S1352-2310(98)00345-8, 1999.

Silvern, R. F., Jacob, D. J., Mickley, L. J., Sulprizio, M. P., Travis, K. R., Marais, E. A., Cohen, R. C., Laughner, J. L., Choi, S., Joiner, J., and Lamsal, L. N.: Using satellite observations of tropospheric NO_2 columns to infer long-term trends in US NO_x emissions: the importance of accounting for the free tropospheric NO_2 background, Atmospheric Chemistry and Physics, 19, 8863–8878, https://doi.org/10.5194/acp-19-8863-2019, 2019.

Soulie, A., Granier, C., Darras, S., Zilbermann, N., Doumbia, T., Guevara, M., Jalkanen, J.-P., Keita, S., Liousse, C., Crippa, M., Guizzardi, D., Hoesly, R., and Smith, S. J.: Global anthropogenic emissions (CAMS-GLOB-ANT) for the Copernicus Atmosphere Monitoring Service simulations of air quality forecasts and reanalyses, Earth System Science Data, 16, 2261–2279, https://doi.org/10.5194/essd-16-2261-2024, 2024.

Souri, A., Nowlan, C., Wolfe, G., Lamsal, N., Miller, C., Gonzalez Abad, G., Janz, S., Fried, A., Blake, D., Weinheimer, A., Diskin, G., Liu, X., and Chance, K.: Revisiting the Effectiveness of HCHO/NO2 Ratios for Inferring Ozone Sensitivity to Its Precursors using High Resolution Airborne Remote Sensing Observations in a High Ozone Episode during the KORUS-AQ Campaign, Atmospheric Environment, https://doi.org/10.1016/j.atmosenv.2020.117341, 2020.

Stauffer, R. M., Thompson, A. M., Kollonige, D. E., Komala, N., Al-Ghazali, H. K., Risdianto, D. Y., Dindang, A., Fairudz bin Jamaluddin, A., Sammathuria, M. K., Zakaria, N. B., Johnson, B. J., and Cullis, P. D.: Dynamical drivers of free-tropospheric ozone increases over equatorial Southeast Asia, Atmospheric Chemistry and Physics, 24, 5221–5234, https://doi.org/10.5194/acp-24-5221-2024, 2024.

Stevenson, D. S., Young, P. J., Naik, V., Lamarque, J.-F., Shindell, D. T., Voulgarakis, A., Skeie, R. B., Dalsoren, S. B., Myhre, G., Berntsen, T. K., Folberth, G. A., Rumbold, S. T., Collins, W. J., MacKenzie, I. A., Doherty, R. M., Zeng, G., van Noije, T. P. C., Strunk, A., Bergmann, D., Cameron-Smith, P., Plummer, D. A., Strode, S. A., Horowitz, L., Lee, Y. H., Szopa, S., Sudo, K., Nagashima, T., Josse,

https://doi.org/10.5194/egusphere-2026-1652
Preprint. Discussion started: 13 May 2026

B., Cionni, I., Righi, M., Eyring, V., Conley, A., Bowman, K. W., Wild, O., and Archibald, A.: Tropospheric ozone changes, radiative forcing and attribution to emissions in the Atmospheric Chemistry and Climate Model Intercomparison Project (ACCMIP), Atmospheric Chemistry and Physics, 13, 3063–3085, https://doi.org/10.5194/acp-13-3063-2013, 2013.

Sun, S., Palmer, P. I., Siddans, R., Kerridge, B. J., Ventress, L., Edtbauer, A., Ringsdorf, A., Pfannerstill, E. Y., and Williams, J.: Seasonal isoprene emission estimates over tropical South America inferred from satellite observations of isoprene, Atmospheric Chemistry and Physics, 25, 15 801–15 818, https://doi.org/10.5194/acp-25-15801-2025, 2025.

Taylor, K. E.: Summarizing multiple aspects of model performance in a single diagram, Journal of Geophysical Research: Atmospheres, 106, 7183–7192, https://doi.org/https://doi.org/10.1029/2000JD900719, 2001.

Theys, N., De Smedt, I., van Gent, J., Danckaert, T., Wang, T., Hendrick, F., Stavrakou, T., Bauduin, S., Clarisse, L., Li, C., Krotkov, N., Yu, H., Brenot, H., and Van Roozendael, M.: Sulfur dioxide vertical column DOAS retrievals from the Ozone Monitoring Instrument: Global observations and comparison to ground-based and satellite data, Journal of Geophysical Research: Atmospheres, 120, 2470–2491, https://doi.org/https://doi.org/10.1002/2014JD022657, 2015.

Thompson, A. M., Stauffer, R. M., Kollonige, D. E., Ziemke, J. R., Cazorla, M., Wolff, P., and Sauvage, B.: Tropical Ozone Trends (1998 to 2023): A Synthesis from SHADOZ, IAGOS and OMI/MLS Observations, EGUsphere, 2025, 1–34, https://doi.org/10.5194/egusphere-2024-3761, 2025.

Tian, Y., Wang, S., and Jin, X.: Global patterns and trends in ground-level ozone chemical formation regimes from 1996 to 2022, Atmospheric Chemistry and Physics, 25, 9127–9149, https://doi.org/10.5194/acp-25-9127-2025, 2025.

van der Werf, G. R., Randerson, J. T., Giglio, L., van Leeuwen, T. T., Chen, Y., Rogers, B. M., Mu, M., van Marle, M. J. E., Morton, D. C., Collatz, G. J., Yokelson, R. J., and Kasibhatla, P. S.: Global fire emissions estimates during 1997–2016, Earth System Science Data, 9, 697–720, https://doi.org/10.5194/essd-9-697-2017, 2017.

Van Malderen, R., Thompson, A. M., Kollonige, D. E., Stauffer, R. M., Smit, H. G. J., Maillard Barras, E., Vigouroux, C., Petropavlovskikh, I., Leblanc, T., Thouret, V., Wolff, P., Effertz, P., Tarasick, D. W., Poyraz, D., Ancellet, G., De Backer, M.-R., Evan, S., Flood, V., Frey, M. M., Hannigan, J. W., Hernandez, J. L., Iarlori, M., Johnson, B. J., Jones, N., Kivi, R., Mahieu, E., McConville, G., Müller, K., Nagahama, T., Notholt, J., Piters, A., Prats, N., Querel, R., Smale, D., Steinbrecht, W., Strong, K., and Sussmann, R.: Global ground-based tropospheric ozone measurements: reference data and individual site trends (2000–2022) from the TOAR-II/HEGIFTOM project, Atmospheric Chemistry and Physics, 25, 7187–7225, https://doi.org/10.5194/acp-25-7187-2025, 2025.

Wang, H., Lu, X., Jacob, D. J., Cooper, O. R., Chang, K.-L., Li, K., Gao, M., Liu, Y., Sheng, B., Wu, K., Wu, T., Zhang, J., Sauvage, B., Nédélec, P., Blot, R., and Fan, S.: Global tropospheric ozone trends, attributions, and radiative impacts in 1995–2017: an integrated analysis using aircraft (IAGOS) observations, ozonesonde, and multi-decadal chemical model simulations, Atmospheric Chemistry and Physics, 22, 13 753–13 782, https://doi.org/10.5194/acp-22-13753-2022, 2022.

Wang, Y., Beirle, S., Lampel, J., Koukouli, M., De Smedt, I., Theys, N., Li, A., Wu, D., Xie, P., Liu, C., Van Roozendael, M., Stavrakou, T., Müller, J.-F., and Wagner, T.: Validation of OMI, GOME-2A and GOME-2B tropospheric NO_2, SO_2 and HCHO products using MAX-DOAS observations from 2011 to 2014 in Wuxi, China: investigation of the effects of priori profiles and aerosols on the satellite products, Atmospheric Chemistry and Physics, 17, 5007–5033, https://doi.org/10.5194/acp-17-5007-2017, 2017.

Wang, Y., Li, K., Chen, X., Yang, Z., Tang, M., Campos, P. M. D., Yang, Y., Yue, X., and Liao, H.: Revisiting the high tropospheric ozone over southern Africa: role of biomass burning and anthropogenic emissions, Atmospheric Chemistry and Physics, 25, 4455–4475, https://doi.org/10.5194/acp-25-4455-2025, 2025.

https://doi.org/10.5194/egusphere-2026-1652
Preprint. Discussion started: 13 May 2026

Wesely, M.: Parameterization of surface resistances to gaseous dry deposition in regional-scale numerical models, Atmospheric Environment (1967), 23, 1293–1304, https://doi.org/https://doi.org/10.1016/0004-6981(89)90153-4, 1989.

Wespes, C., Hurtmans, D., Emmons, L. K., Safieddine, S., Clerbaux, C., Edwards, D. P., and Coheur, P.-F.: Ozone variability in the troposphere and the stratosphere from the first 6 years of IASI observations (2008–2013), Atmospheric Chemistry and Physics, 16, 5721–5743, https://doi.org/10.5194/acp-16-5721-2016, 2016.

West, J. J. and Fiore, A. M.: Management of Tropospheric Ozone by Reducing Methane Emissions, Environmental Science & Technology, 39, 4685–4691, https://doi.org/10.1021/es048629f, pMID: 16053064, 2005.

Whaley, C. H., Strong, K., Jones, D. B. A., Walker, T. W., Jiang, Z., Henze, D. K., Cooke, M. A., McLinden, C. A., Mittermeier, R. L., Pommier, M., and Fogal, P. F.: Toronto area ozone: Long-term measurements and modeled sources of poor air quality events, Journal of Geophysical Research: Atmospheres, 120, 11,368–11,390, https://doi.org/https://doi.org/10.1002/2014JD022984, 2015.

WHO: Health aspects of air pollution with particulate matter, ozone and nitrogen dioxide: report on a WHO working group, Bonn, Germany 13-15 January 2003, in: Health aspects of air pollution with particulate matter, ozone and nitrogen dioxide: report on a WHO working group, Bonn, Germany 13-15 January 2003, 2003.

Wiedinmyer, C., Akagi, S. K., Yokelson, R. J., Emmons, L. K., Al-Saadi, J. A., Orlando, J. J., and Soja, A. J.: The Fire INventory from NCAR (FINN): a high resolution global model to estimate the emissions from open burning, Geoscientific Model Development, 4, 625–641, https://doi.org/10.5194/gmd-4-625-2011, 2011.

Wiedinmyer, C., Kimura, Y., McDonald-Buller, E. C., Emmons, L. K., Buchholz, R. R., Tang, W., Seto, K., Joseph, M. B., Barsanti, K. C., Carlton, A. G., and Yokelson, R.: The Fire Inventory from NCAR version 2.5: an updated global fire emissions model for climate and chemistry applications, Geoscientific Model Development, 16, 3873–3891, https://doi.org/10.5194/gmd-16-3873-2023, 2023.

Young, P. J., Naik, V., Fiore, A. M., Gaudel, A., Guo, J., Lin, M. Y., Neu, J. L., Parrish, D. D., Rieder, H. E., Schnell, J. L., Tilmes, S., Wild, O., Zhang, L., Ziemke, J., Brandt, J., Delcloo, A., Doherty, R. M., Geels, C., Hegglin, M. I., Hu, L., Im, U., Kumar, R., Luhar, A., Murray, L., Plummer, D., Rodriguez, J., Saiz-Lopez, A., Schultz, M. G., Woodhouse, M. T., and Zeng, G.: Tropospheric Ozone Assessment Report: Assessment of global-scale model performance for global and regional ozone distributions, variability, and trends, Elementa: Science of the Anthropocene, 6, 10, https://doi.org/10.1525/elementa.265, 2018.

Zhang, Y., Cooper, O., Gaudel, A., Thompson, A., Nédélec, P., Ogino, S.-Y., and West, J.: Tropospheric ozone change from 1980 to 2010 dominated by equatorward redistribution of emissions, Nature Geoscience, 9, https://doi.org/10.1038/ngeo2827, 2016.

Zhang, Y., Yu, H., De Smedt, I., Lin, J., Theys, N., Van Roozendael, M., Pinardi, G., Compernolle, S., Ni, R., Ren, F., Wang, S., Chen, L., Van Geffen, J., Liu, M., Cede, A. M., Tiefengraber, M., Merlaud, A., Friedrich, M. M., Richter, A., Piters, A., Kumar, V., Sinha, V., Wagner, T., Choi, Y., Takashima, H., Kanaya, Y., Irie, H., Spurr, R., Sun, W., and Fabris, L.: Global retrieval of TROPOMI tropospheric HCHO and NO_2 columns with improved consistency based on the updated Peking University OMI NO_2 algorithm, Atmospheric Measurement Techniques, 18, 1561–1589, https://doi.org/10.5194/amt-18-1561-2025, 2025.

Zheng, B., Tong, D., Li, M., Liu, F., Hong, C., Geng, G., Li, H., Li, X., Peng, L., Qi, J., Yan, L., Zhang, Y., Zhao, H., Zheng, Y., He, K., and Zhang, Q.: Trends in China's anthropogenic emissions since 2010 as the consequence of clean air actions, Atmospheric Chemistry and Physics, 18, 14 095–14 111, https://doi.org/10.5194/acp-18-14095-2018, 2018.

Zhu, L., Jacob, D. J., Kim, P. S., Fisher, J. A., Yu, K., Travis, K. R., Mickley, L. J., Yantosca, R. M., Sulprizio, M. P., De Smedt, I., González Abad, G., Chance, K., Li, C., Ferrare, R., Fried, A., Hair, J. W., Hanisco, T. F., Richter, D., Jo Scarino, A., Walega, J., Weibring, P., and Wolfe, G. M.: Observing atmospheric formaldehyde (HCHO) from space: validation and intercomparison of six retrievals from four

https://doi.org/10.5194/egusphere-2026-1652
Preprint. Discussion started: 13 May 2026

satellites (OMI, GOME2A, GOME2B, OMPS) with SEAC^{4}RS aircraft observations over the southeast US, Atmospheric Chemistry and Physics, 16, 13 477–13 490, https://doi.org/10.5194/acp-16-13477-2016, 2016.

Ziemke, J. R., Chandra, S., Duncan, B. N., Schoeberl, M. R., Torres, O., Damon, M. R., and Bhartia, P. K.: Recent biomass burning in the tropics and related changes in tropospheric ozone, Geophysical Research Letters, 36, https://doi.org/https://doi.org/10.1029/2009GL039303, 2009.

Ziemke, J. R., Oman, L. D., Strode, S. A., Douglass, A. R., Olsen, M. A., McPeters, R. D., Bhartia, P. K., Froidevaux, L., Labow, G. J., Witte, J. C., Thompson, A. M., Haffner, D. P., Kramarova, N. A., Frith, S. M., Huang, L.-K., Jaross, G. R., Seftor, C. J., Deland, M. T., and Taylor, S. L.: Trends in global tropospheric ozone inferred from a composite record of TOMS/OMI/MLS/OMPS satellite measurements and the MERRA-2 GMI simulation, Atmospheric Chemistry and Physics, 19, 3257–3269, https://doi.org/10.5194/acp-19-3257-2019, 2019.